AGU ADVANCING EARTH AND SPACE SCIENCE

Water Resources Research

RESEARCH ARTICLE
10.1029/2020WR029266

Variable 21st Century Climate Change Response for Rivers in High Mountain Asia at Seasonal to Decadal Time Scales

S. Khanal[1,2], A.F. Lutz[2,3], P. D. A. Kraaijenbrink[3], B. van den Hurk[1,4], T. Yao[5], and W. W. Immerzeel[3]

[1]Vrije University, Institute for Environmental Research, Amsterdam, The Netherlands, [2]FutureWater, Wageningen, The Netherlands, [3]Utrecht University, Department of Physical Geography, Utrecht, The Netherlands, [4]Deltares, Delft, The Netherlands, [5]Key Laboratory of Tibetan Environmental Changes and Land Surface Processes, Institute of Tibetan Plateau Research, Chinese Academy of Sciences, Beijing, China

Key Points:

- Contrasting seasonal responses are observed for High Mountain Asia's (HMA) rivers, dictated by their hydrological regimes
- The onset of early snow and glacier melt in the spring season affects the magnitude and peak water availability
- A relatively consistent decadal climate change responses across HMA, despite a large variability in hydrological regimes

Supporting Information:

Supporting Information may be found in the online version of this article.

Correspondence to:

S. Khanal,
s.khanal@futurewater.nl

Citation:

Khanal, S., Lutz, A. F., Kraaijenbrink, P. D. A., van den Hurk, B., Yao, T., & Immerzeel, W. W. (2021). Variable 21st century climate change response for rivers in High Mountain Asia at seasonal to decadal time scales. *Water Resources Research*, *57*, e2020WR029266. https://doi.org/10.1029/2020WR029266

Received 21 NOV 2020
Accepted 8 MAY 2021

Abstract The hydrological response to climate change in mountainous basins manifests itself at varying spatial and temporal scales, ranging from catchment to large river basin scale and from sub-daily to decade and century scale. To robustly assess the 21st century climate change impact for hydrology in entire High Mountain Asia (HMA) at a wide range of scales, we use a high resolution cryospheric-hydrological model covering 15 upstream HMA basins to quantify the compound effects of future changes in precipitation and temperature based on the range of climate change projections in the Coupled Model Intercomparison Project Phase 6 climate model ensemble. Our analysis reveals contrasting responses for HMA's rivers, dictated by their hydrological regimes. At the seasonal scale, the earlier onset of melting causes a shift in the magnitude and peak of water availability, to earlier in the year. At the decade to century scale, after an initial increase, the glacier melt declines by the mid or end of the century except for the Tarim river basin, where it continues to increase. Despite a large variability in hydrological regimes across HMA's rivers, our results indicate relatively consistent climate change responses across HMA in terms of total water availability at decadal time scales. Although total water availability increases for the headwaters, changes in seasonality and magnitude may diverge widely between basins and need to be addressed while adapting to future changes in a region where food security, energy security as well as biodiversity, and the livelihoods of many depend on water from HMA.

Plain Language Summary The mountains of Asia have large reservoirs of snow and ice, which are the source of water to the people living in the mountains and downstream, mainly during the dry season. However, due to recent warming, these reserves are melting faster and depleting year by year. We use a computer model to understand what will happen to these volumes of snow and ice and the total volume of water, which also includes rain and groundwater, in the 15 main rivers under future climate change scenarios. We find that the water generated upstream will increase for all the rivers in the future. However, there would be either too little or too much water for different seasons in the future. The peak volume of water will increase in magnitude and the peak time will shift to earlier in the season (in the month of May instead of current June or July) for most rivers in the western part of Asia. This change in the timing of water will have severe impacts on the livelihoods of mountain communities as well as populations downstream where food production, energy production as well as biodiversity depend on the amount and timing of mountain water supply.

1. Introduction

High Mountain Asia (HMA) has the world's largest ice and snow reserves outside the polar regions and is an important source of water for the major river systems in Asia, providing water for a population of more than a billion people, which is increasing rapidly (Immerzeel, 2010; Immerzeel et al., 2020; Stocker et al., 2013). The HMA region is characterized by contrasting atmospheric circulation patterns (Bookhagen & Burbank, 2006; Cannon et al., 2016). Midlatitude westerlies and Asian monsoon systems supply most moisture as snow or rain in the western and eastern parts of HMA, respectively. The variability in the

climate, hypsometry, and cryosphere distribution leads to characteristic glacial, nival, pluvial, and mixed hydrological regimes in HMA's rivers.

In the past decades, HMA has experienced many climatic changes (Krishnan et al., 2019; Yan & Liu, 2014; Zhan et al., 2017). Past climate change led to changes in the cryosphere and hydrological cycle (Bolch et al., 2012; Kang et al., 2010; King et al., 2019; Sakai & Fujita, 2017; Yao et al., 2012). These changes include rapid glacier shrinkage, reduction in snow cover, permafrost degradation, changes in area of seasonally frozen grounds, and increases in the frequency of snow and ice avalanches (Ballesteros-Cánovas et al., 2018; Bolch et al., 2012; Kang et al., 2010). The changes in climate and cryosphere lead to shifts in timing and magnitude of river discharge (Immerzeel, 2010; Lutz et al., 2014; Maurer et al., 2019). Furthermore, climate change lead to increases in area and volume of glacial lakes has further exacerbated the risk of glacial lake outburst floods (King et al., 2019; Liu et al., 2014; Zhang et al., 2015).

In the future, climate change is expected to lead to further changes in cryospheric storages and subsequently impact the hydrological cycle (Kraaijenbrink et al., 2017; Lutz et al., 2014; Maurer et al., 2019; Wijngaard et al., 2017). The climate change response of different hydrological processes depends strongly on spatio-temporal scales and varies from catchment to river basin scale and sub-daily to decadal time scales (Hock, Rasul, et al., 2019). While rainfall-runoff processes respond quickly to climatic changes, glacier melt generation responds at longer time scales of decades to centuries and strongly depends on the presently available ice volume and the time scale considered. As long as sufficient ice is present, further warming will continue to increase glacier melt, but a decreasing glacier area will lead to a gradual reduction of melt generation in the long run. The time it takes to reach the melt peak increases with ice volume (Huss & Hock, 2018). For snow, different processes combine in response to warming: a higher temperature accelerates snowmelt but reduces the fraction of precipitation that falls as snow, which eventually will lead to a decrease of snowmelt as a contributor to total runoff. The response time for snow processes under climate change varies from seasonal to annual time scales. Via compensating and contrasting impacts of precipitation and temperature on the discharge volume from the HMA headwaters, changes in these climatic variables give rise to nonlinear, non-stationary, and non-uniform responses of cryospheric and hydrological variables such as snow, glaciers, soil moisture, and groundwater, at varying spatial and temporal scales (Blöschl et al., 2017; Hall et al., 2014). The systemic effect of the compound occurrence of extreme precipitation and temperature and their impacts on the seasonality and trends in total water availability for HMA is largely unresolved (Zscheischler et al., 2018, 2020; Zscheischler & Seneviratne, 2017).

Recent studies have focused on glacier melt to derive the impact of either historical or future climate change on melt water availability on a regional and global scale (Brun et al., 2017; Hock, Bliss, et al., 2019; Huss & Hock, 2018; Kaser et al., 2010; Kraaijenbrink et al., 2017; Marzeion et al., 2020; Maurer et al., 2019). Many studies have investigated the impact of historical and future climate change on the melt water and streamflow contributors in HMA for fragmented regions varying from sub-basin to basin-scale (Immerzeel, 2008; Immerzeel et al., 2013; Lutz et al., 2016; Nepal, 2016; Ragettli et al., 2016; Sorg et al., 2014). Only a few studies have investigated the impact of climate change on streamflow contributors (i.e., hydrological regime) on a regional scale in HMA (Armstrong et al., 2019; Immerzeel, 2010; Lutz et al., 2014; Miller et al., 2012; Wijngaard et al., 2017). These basin-scale and regional studies use different data and approaches. Variability in approaches, data, and methods makes it difficult to align and compare the effects of climate change on future melt contribution and water availability across HMA. A consistent, high-resolution, long-term modeling approach is required for a robust and spatially consistent assessment of climate change impacts for cryospheric and hydrological processes and their states in HMA at different spatial and temporal scales.

In this study, we bridge scale, variability in approaches, data, and methodological issues by implementing a consistent large-scale high-resolution cryospheric-hydrological model for the entire HMA region to simulate the impacts of climate change on the hydrological cycle at varying spatial and temporal scales. First, we simulate hydrological processes for the historical climate and categorize river basins by their hydrological regimes based on the contribution of glacier, snow, and rainfall-runoff for 15 upstream basins. Second, we assess the compound impact of changes in precipitation and temperature on peak water availability and shifts in these hydrological regimes for different combinations of future climatic changes. Third, we assess the seasonal and decadal changes in hydrological processes for different hydrological regimes. Last, we investigate the changes in total water availability for different spatial scales.

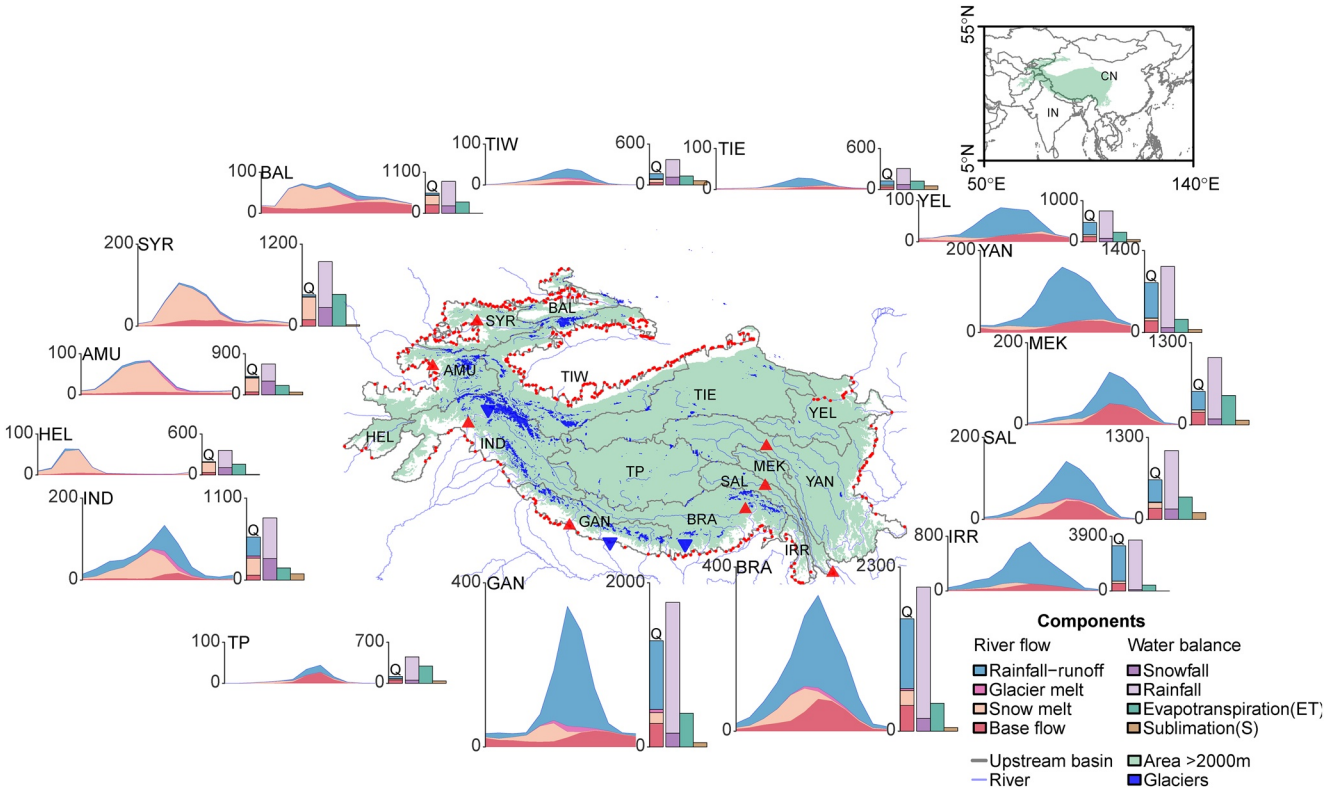

Figure 1. The upstream mountainous basins of High Mountain Asia analyzed in this study (gray boundaries). The green color represents the area above 2,000 m. Shown are 1985–2014 mean seasonal cycles of discharge (Q, in mm yr^{-1}) contributed by baseflow (red), snowmelt (orange), glacier melt (magenta), and rainfall-runoff (blue). Stacked bar plots aside show the average annual contributions of the discharge components (Q, first bar), the precipitation (P, second bar) falling as rain (light purple) and snow (purple), the actual evapotranspiration (light green, third bar), and sublimation (brown, fourth bar). The red triangles in the geographical map represent the station locations used for the calibration and validation of the hydrological model with observed discharge. The blue downward triangles represent the station locations where independent model validation with observed discharge is performed. Note the difference in vertical scale for each of the basins.

2. Study Area

We define HMA as the region within 57°–113°E and 22°–47°N encompassing the Tibetan Plateau and the adjacent mountain ranges Tien Shan, Pamir, Hindu Kush, and Karakoram in the West, the Himalayas in the south and southeast and Qilian Shan in the East. We focus our analysis on the high-altitude upstream parts of 15 major river basins in HMA (Figure 1). The upstream region defined in this study includes all areas above 2,000 m asl (meters above sea level) (details in supporting information Text S1). The HMA region has strong longitudinal (West-East), latitudinal (North-South), and vertical climate gradients, therefore making the climate highly diverse (Figure 2). The 15 upstream river basins analyzed in this study are the Amu Darya (AMU), Balkash (BAL), Brahmaputra (BRA), Ganges (GAN), Helmand (HEL), Indus (IND), Irrawaddy (IRR), Mekong (MEK), Plateau of Tibet Interior (TP), Salween (SAL), Syr Darya (SYR), Tarim interior east (TIE) Tarim interior west (TIW), Yangtze (YAN), Yellow (YEL) (Figure 1). Overall, the HMA region includes 97,590 glaciers covering 98,534 km^2 (Farinotti et al., 2019). The IND and TIW basins have the highest glaciated area covering over 29,700 km^2 (6.3% of total upstream basin area) and 27,700 km^2 (5.8%) (Figure 2).

3. Data and Methods

3.1. Glacio-Hydrological Model

In this study, we use the Spatial Processes in Hydrology (SPHY) v3 model, which is a spatially distributed (raster-based) "leaky-bucket" type water balance model (Terink et al., 2015). The model is designed for large scale cryospheric-hydrological studies and integrates different hydrological processes, including (a)

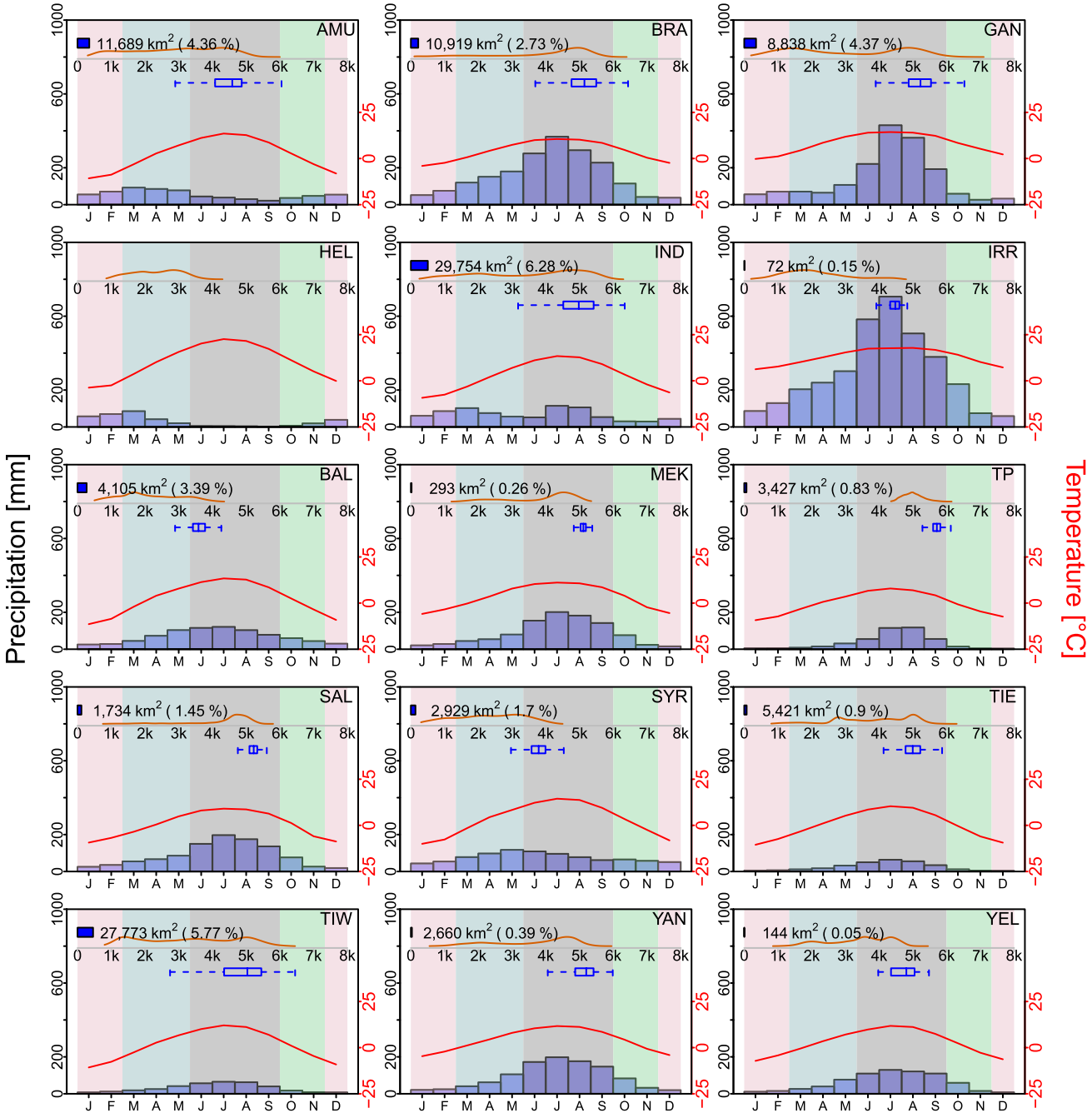

Figure 2. Climate setting and relevant characteristics of each basin. The blue histogram (bottom half) represents the average monthly precipitation for the full ERA5 period (1979–2018). The red line (bottom half) represents the average monthly temperature for the same period (right axis). The orange line (top half) represents the elevation distribution of the upper basins (scaled between 0 and 1 on the *y*-axis). The horizontal blue box plot (top half) represents the elevation distribution of the glaciers in the basins (except HEL). The width of the blue bar (top left) represents the percentage of glacierized area relative to the total upstream basin area (scaled to 0%–100% on the *x*-axis). The text on the right of the blue bar (top left) gives the total glacier area (km^2) and the number in parenthesis gives the percentage of glacier area relative to the upstream basin area. The pale background color represents four seasons: winter (DJF), spring (MAM), monsoon (JJAS), and autumn (ON).

rainfall-runoff, (b) cryospheric processes, (c) evapotranspiration, and (d) soil hydrological processes. SPHY can operate at flexible spatial scales (sub-basin, basin, and regional).

For this study, the model runs at a daily time step at 5 × 5 km spatial resolution covering 15 upstream river basins in HMA. The total runoff (Q_{Tot}) for each grid cell at any time step in the model is the sum of glacier-melt runoff (Q_{GM}), snowmelt runoff (Q_{SM}), rainfall-runoff (Q_{RR}), and baseflow (Q_{BF}).

$$Q_{Tot} = \Sigma\left(Q_{GM}, Q_{SM}, Q_{RR}, Q_{BF}\right) \quad (1)$$

For each grid cell, a dynamic snow storage, soil water storage, and ground water storage are maintained. Snow melt runoff is calculated for the snow-covered grid cell over the land surface. The snow melt runoff over the glacier surface is defined as glacier runoff. A degree-day approach with calibrated melt rates is used to calculate the snowmelt. For each time step, before melt is calculated, sublimation is estimated using a large-scale parameterization for sublimation and removed from the snow storage. Subsequently, snow melt is calculated and removed from the snow storage at each time step. The model also accounts for the refreezing of melt water within the snowpack. When the snow melt exceeds the storage threshold, snow melt runoff is generated. Rainfall-runoff is calculated as the sum of surface runoff from rainfall and lateral flow from the soil water storage layer. Surface runoff is calculated based on saturation excess runoff. The reference evapotranspiration is calculated using the Modified Hargreaves reference evapotranspiration method (Hargreaves & Samani, 1985). The resulting soil moisture, depending on the soil properties, is subjected to evapotranspiration, influenced by the land use type and capillary rise, while the remainder (if any) contributes to the river discharge through lateral flow or surface runoff. The ground water storage releases delayed baseflow runoff. Each of these runoff types are routed downstream using a simple recession coefficient method. While the runoff contributors are self-explanatory, in the next section we discuss the glacier module in detail.

3.1.1. Dynamic Glacier Module

The model takes sub-grid variability into account by calculating the snow and glacier melt runoff from glaciers at a 50 × 50 m sub-grid. By intersecting the Randolph Glacier Inventory glacier outlines with the 5 × 5 km model grid, we identify the glaciers or parts thereof (fraction) that lie within each model grid cell (RGI Consortium, 2017). Each (part of a) glacier is assigned a unique-id. To simulate future changes in glaciers, we simulate the glacier mass balance of each individual glacier, which can occupy multiple model grid cells. We distinguish debris-covered and debris-free parts for each glacier based on the classification by Kraaijenbrink et al. (2017). We assign the initial ice thickness and volume for each (part of a) glacier parts using ice volume data from Farinotti et al. (2019). For each (part of a) glacier, we derive its mean elevation from a 30 × 30 m digital elevation model, to lapse daily air temperature from the 5 × 5 km model grid cell mean elevation to the glacier's mean elevation (Farr et al., 2007). Daily precipitation and temperature serve as input for the glacier module to calculate accumulation and melt. The module uses a degree-day approach to calculate the glacier ice melt (Hock, 2003). Different calibrated melt rates are applied to debris-covered and debris-free glaciers (Bolch et al., 2012; Gardelle et al., 2013; Scherler et al., 2011). Future changes in (parts of) glaciers in response to the precipitation and temperature are taken into account by using a mass conserving ice redistribution approach. The ice redistribution is done once per year at the end of the hydrological year, which is also the end of the melting season (October 1st). At that moment the accumulated snow in the accumulation zone is transformed into ice and distributed downwards to the ablation area. The net imbalance (I), that is, the difference in the volume of total snow accumulated ($SnowS$) and total volume of melt generated from the glaciers (GM), forms the basis of ice redistribution:

$$I_{n,j} = SnowS_{n,j} - GM_{n,j} \quad (2)$$

where the subscript n is the glacier id, and j is a unique-id. Only when the net imbalance is negative, the volume of ice is redistributed (Vred) over the ablation zone according to:

$$Vred_{n,j} = \begin{cases} 0 & , \quad j \epsilon B_{n,j} \\ \sum_{j \epsilon B_{n,j}} I_{n,j} \times \frac{Vini_{n,j}}{\sum_{j \epsilon A_{n,j}} Vini_{n,j}} & , \quad j \epsilon A_{n,j} \end{cases} \tag{3}$$

where *Aj* is the part of the glacier with a negative imbalance, *Bj* is the part of the glacier with a positive imbalance in any glacier-id *n*. The redistribution is proportional to the initial total volume of ice (*V*ini), that is, glacier parts with a larger initial ice volume will receive a large volume of accumulated ice from the accumulation zone to the ablation zone.

3.1.2. Snow Sublimation

We use a large-scale parameterization to estimate the sublimation from the snow storage. Although snow sublimation is an essential component of the water balance in mountainous regions, its magnitude is still uncertain and poorly understood (Stigter et al., 2018). To understand and quantify sublimation from snow, we use an estimate of the theoretical incoming shortwave radiation, the topographic exposure to wind calculated based on the angle of inflection, and elevation (Fu & Rich, 1999; Winstral & Marks, 2002). We calculate the monthly probability of sublimation (P_{sub}) as:

$$P_{sub} = SW \times \left(1 - e\right) \times h \tag{4}$$

where *SW* is the incoming shortwave radiation in W m^{-2}, *e* is topographic exposure, a dimensionless number which ranges between 0 and 275, and *h* is the elevation in m. The elevation is scaled between 2,500 and 6,500 m to restrict the snow sublimation. The resulting P_{sub} is further scaled between 0 and 1; with higher values indicating a higher probability of sublimation. The theoretical maximum sublimation (*S*max) is calculated as:

$$Smax = \left(1 - \alpha\right) \times SW \times L \tag{5}$$

where, α is albedo (a unitless number varying from 0 to 1), and *L* is the latent heat of sublimation (2.838 kJ kg^{-1}). Sublimation is strongly dependent on wind, temperature, and humidity (Hood et al., 1999). There are several constraints to the conditions favorable for sublimation; for instance, the melting snow surface temperature cannot exceed 0°C, and vapor partial pressure at the surface cannot exceed 6.11 hPa (Strasser et al., 2008). Here, we use a proxy of humidity conditions by assuming low precipitation intensity ($P < 1$ mm d^{-1}) to be favorable for the sublimation to occur. The favorable sublimation condition (*S*con) in the model is calculated as:

$$Scon = \left(T <= 0\right) \& \left(SnowS > 0\right) \& \left(P <= 1\right) \tag{6}$$

where *T* is the mean air temperature, *SnowS* is the snow storage (mm), and *P* is the precipitation (mm). *Scon* is a binary value where 0 represents grid cells with no sublimation, and 1 represents grid cells with sublimation.

Finally, the actual sublimation (*S*act) is calculated as:

$$Sact = Sfact \times Scon \times P_{sub} \times Smax \tag{7}$$

where the sublimation factor (*S*fact) is a calibration parameter that ranges between 0 and 1.

3.2. Data

3.2.1. Climate Data

The SPHY model is forced with precipitation and temperature fields from the European Center for Medium-Range Weather Forecasts (ECMWF) ERA5 climate data (Hersbach et al., 2020). The ERA5 data are

available for 1979–2018 at an hourly time scale and 31 × 31 km spatial resolution (hereafter referred to as ERA5 resolution). ERA5 hourly precipitation is aggregated to daily precipitation sum and then interpolated to 5 × 5 km model grid using a cubic spline interpolation. Similarly, mean, maximum (max), and minimum (min) daily temperature aggregates were created from the hourly ERA5 data and spatially resampled using a cubic spline interpolation. The resampled temperature fields (T_{cor}) are spatially downscaled using the digital elevation model (DEM, see Section 3.2.3) and vertical temperature lapse rates (VLR). A linear regression method is applied to calculate the monthly VLR from ERA5 temperature climatology at the original ERA5 resolution for a 5 × 5 grid cell window around each grid cell in the model domain. The resampled monthly vertical lapse rates are then aggregated over the basins and used to correct air temperature at 5 × 5 km model resolution as in Equation 8.

$$T_{\mathrm{cor},t} = T_{\mathrm{res},t} \times \mathrm{VLR}_{m,t} \times \left(h1 - h2\right) \tag{8}$$

where $T_{cor,t}$ is the corrected temperature at time step t, $T_{res,t}$ is the resampled temperature from ERA5 resolution to model resolution, VLR_t is the resampled vertical lapse rate for a corresponding month (m), $h1$ is the elevation aggregated to 5 × 5 km model resolution, and $h2$ is elevation aggregated to the original ERA5 grid resolution and smoothed to the model resolution.

We used projected changes in temperature (dT) and precipitation (dP) from the Coupled Model Intercomparison Project Phase 6 ensemble (CMIP6) to generate the future climate forcing (Eyring et al., 2016). Several recent studies have investigated dP and dT in the Asian and Tibetan plateau regions with the available CMIP6 models (Almazroui et al., 2020; Na et al., 2020). Based on the ranges in the projections of the CMIP6 ensemble for these regions, we select −30% to +40% for dP and 3°C to 8°C for dT as change by the end of the century (2100) compared to the reference period. Over these ranges, increments of 1°C for dT and 10% for dP were used to generate 48 different combinations of future climate change projections. The dT and dP in each combination were assumed to change linearly between the start of the century (2015) and the end of the century (2100). Future time episodes are generated by random sampling from the full ERA5 years historical model forcing (1979–2018) without replacement, in three blocks of 40 years each, to generate a transient sequence of 86 years (2015–2100). The annual incremental increase (or decrease) is added to the temperature fields and multiplied with the precipitation fields to generate the future forcing for corresponding daily time steps of the resampled years. In this way, we generate transient future forcing for the entire region, from 2015 until 2100, for the 48 different future combinations.

For parts of the analysis, we categorize the 48 climate runs in to four groups of 12 combinations each; warm-wet (dT from 6°C to 8°C, dP from 10% to 40%), cold-wet (dT from 3°C to 5°C, dP from 10% to 40%), warm-dry (dT from 6°C to 8°C, dP from −30% to 0%) and cold-dry (dT from 3°C to 5°C, dP from −30% to 0%) (supplementary Figure S1). Any positive (negative) increment in precipitation is defined as a wet (dry) scenario. Further, a distinction is made for a wet (dry) scenario, based on the temperature either as cold-wet (cold-dry) or warm-wet (warm-dry) (Lutz et al., 2016). While the wet scenarios (i.e., positive precipitation increment) are self-explanatory, the temperature scenarios were distributed evenly (3°C to 5°C as cold and 6°C to 8°C as warm). To show the seasonal and decadal changes for different hydrological regimes, we focus on three specific future runs: high dT (dT = 8°C and dP = +0%), high dP (dT = 3°C and dP = +30%), and high dPdT (dT = 8°C and dP = +30%).

Unless explicitly specified, we use 30 years (1985–2014) as a reference period throughout the study. To investigate the climate change impacts in the future, we divide the future period into two slices of 30 years; mid-century (hereafter referred to as MC, 2036–2065) and end of century (hereafter referred to as EOC, 2071–2100). Furthermore, to assess seasonal changes, we divide the year into four seasons: winter (from December to February, DJF), spring/premonsoon (from March to May, MAM), summer/monsoon (from June to September, JJAS), and autumn/postmonsoon (October and November, ON).

3.2.2. Discharge Data

The discharge data in this study were obtained from the Nepal Department of Hydrology and Meteorology (DHM), Pakistan Water and Power Development Authority (WAPDA), Bhutan National Center of

Table 1
The Stations Used for the Calibration and Validation in This study

Basin	Names	Station	Calibration period	Validation period	Missing years	Frequency	Data source	Type
Amu Darya	AMU	Nurek inflow	2001–2004	2005–2010	–	Daily flows	CAWATER	C,V
Brahmaputra	BRA	Nu Xia	1979–1982	–	–	Daily flows	GRDC	C
Brahmaputra	BRA	Wangdirapids	–	2004–2008	–	Daily flows	NCHM	IV
Ganges	GAN	Chisapani	2001–2004	2011–2014	–	Daily flows	DHM	C,V
Ganges	GAN	Devghat	2001–2004	2011–2014	–	Daily flows	DHM	IV
Indus*	IND	Dainyor bridge	2001–2004	2006–2010	2005–2007	Daily flows	WAPDA	IV
Indus	IND	Tarbela inflow	2001–2004	2006–2010	–	Daily flows	WAPDA	C,V
Mekong*	MEK	Jiajiu	1979–1983	1984–1987	1986	Daily flows	GRDC	C,V
Salween*	SAL	Jia yu qiao	1980–1983	1984–1987	1981,1983,1986	Daily flows	GRDC	C,V
Syr Darya	SYR	Toktogul	2001–2004	2005–2010	–	Daily flows	CAWATER	C,V
Yangtze	YAN	Zhimenda	1981–1985	1990–1997	–	Daily flows	GRDC	C,V

The type "C", "V", and "IV" indicates calibration, validation, and independent validation. The basins with * represent the missing year in the discharge time series.

Abbreviations: AMU, Amu Darya; BRA, Brahmaputra; DHM, Department of Hydrology and Meteorology; GAN, Ganges; GRDC, Global Runoff Data Center; IND, Indus; MEK, Mekong; NCHM, National Center of Hydrology and Meteorology; SAL, Salween; SYR, Syr Darya; WAPADA, Water and Power Development Authority; YAN, Yangtze.

Hydrology and Meteorology (NCHM), Central Asian Waterinfo portal (CAWater, 2020) and Global Runoff Data Center (GRDC, 2020) as shown in Table 1.

3.2.3. Other Data

We use the hydrologically conditioned 30 arc-second resolution (~1 km) DEM from HydroSHEDS, resampled to 5 × 5 km model resolution in order to calculate the slope, cell drainage direction, and for lapsing of temperature fields (Lehner et al., 2008). We also use the 1 arcsec (~30 m) Shuttle Radar Topography Mission (SRTM) elevation data to calculate the mean glacier elevation used for the glacier melt calculation (Farr et al., 2007). The MODIS MOD10CM006 (hereafter referred to as MODIS) snow cover data (2001–2017) is used to calculate the monthly snow persistence (Hall & Riggs, 2015). The glacier outlines defined in RGI6.0 for the RGI regions 13 (Central Asia), 14 (South Asia West), and 15 (South Asia East) were used in this study (RGI Consortium, 2017). The initial ice thicknesses for individual glaciers are derived from modeled glacier ice depths (Farinotti et al., 2019). Geodetic glacier mass balance data (Brun et al., 2017) is used to calibrate snow and glacier melt parameters over glaciers. Hydrological subbasin boundaries from HydroBasins data set (referred to as hydro-basins) at spatial level 05 are used to aggregate specific glacier melt to hydrological units for model calibration purposes (Lehner & Grill, 2013). Hydraulic soil properties used in this study were derived from HiHydroSoil (1 × 1 km) and resampled to model resolution (Böer, 2016). Land use data used in the model are derived from the European Space Agency Climate Change Initiative (ESA CCI) data set (Kirches et al., 2014).

3.3. Methods

3.3.1. Bias Correction of ERA5 Temperature Data

Several studies have found a cold bias in ERA5 temperature in mid-latitudes and on the TP (Cao et al., 2020; Ji & Yuan, 2020; Orsolini et al., 2019; Yan et al., 2019). Cold biases in the order of 5°C during winter months have been reported in the eastern part of the TP (Yan et al., 2019). We used MODIS-derived snow persistence to bias correct the temperature fields in ERA5. Snow persistence is defined as the fraction of time that a grid cell is covered by snow. The SPHY model is run from 2001 to 2017, and the temperature is corrected for individual grid cells to match the simulated snow persistence from SPHY to observed snow persistence from MODIS. We use a minimum threshold of 5 mm of snow storage to limit the very shallow and infrequent snow cover in SPHY. Parameters related to snow processes in SPHY; the critical snow temperature (*T*crit),

which controls the snow and rain differentiation, and degree-day factor for snow (DDFs), were assumed to be 0 and 4.5 mm°C^{-1} day^{-1} (supplementary Table S1). We aggregate the snow persistence from SPHY and MODIS to a 100 × 100 km grid and calculate the difference in snow persistence. We iteratively increase the temperature fields by +1°C until the difference in snow persistence from SPHY and MODIS is within ±10%. We only implement a one-way bias correction, to a maximum of +5°C consistent with the reported cold bias over the TP. The bias-correction factors are spatially smoothed from 100 × 100 to 5 × 5 km model resolution.

3.3.2. Model Calibration

To avoid the pitfalls of model equifinality, we use a three-step modeling strategy to calibrate the snow, glaciers, and rainfall-runoff processes in the model (Pellicciotti et al., 2012). First, parameters related to snow processes are calibrated to observed MODIS snow cover data. Second, parameters related to glacier melt are calibrated to observed geodetic glacier mass balance data. Third, rainfall-runoff and routing parameters are calibrated to observed streamflow (supplementary Table S1).

3.3.2.1. Snow Cover Calibration

After the bias-correction of the temperature fields, we calibrate *S*fact in the sublimation routine for each upstream basin to optimize simulated snow cover. *S*fact is optimized to minimize the difference between the mean annual simulated and observed snow persistence in SPHY and MODIS, respectively (supplementary Table S1). Here, we use a maximum ±10% difference in snow persistence as an optimization target for the calibration.

3.3.2.2. Glacier Mass Balance Calibration

The geodetic glacier mass balance database from Brun et al. (2017) is used as the observed mass balance data (hereafter "observed") to calibrate the glacier melt parameters; debris-free (DDF_{ci}) and debris-covered (DDF_{dc}). The observed database consists of mass balance information of 92% of the glaciers in HMA for period 2000 to 2016.

In the first step, the melting factors (DDF_{ci} and DDF_{dc}) for glaciers are adjusted. DDF_{dc} and DDF_{ci} are assumed to be proportional as shown in 9.

$$\mathrm{DDF_{dc}} = 0.2 \times \mathrm{DDF_{ci}} \tag{9}$$

Factor 0.2 is incorporated to represent the reduced melting rates of debris-covered glaciers relative to debris-free glaciers (Östrem, 1959). DDF_{ci} is varied between 3 and 7 mm°C^{-1} day^{-1}, consistent with melt rates found in other studies in the region (Braithwaite, 2008; Immerzeel et al., 2012; Singh et al., 2000; Zhang et al., 2006). For each run from 2001 to 2017, the simulated glacier area-specific mass balance is calculated and compared with the observed area-specific mass balance data. We calibrate at the spatial aggregation level of sub-basins, as defined by the level 05 data in the hydro-basins data set (supplementary Figure S2). The DDF values are optimized until the difference between observed and simulated glacier mass balance is within ±0.05 m w.e yr^{-1}. Where calibration of degree-day factors does not lead to sufficient accuracy in the simulation of the glacier mass balance, we calibrate the glacier VLR used in the glacier melt calculation. The initial monthly VLRs used in the glacier module are estimated from the ERA5 described in Section 3.2.1. The range of the VLR after calibration is confined between 0 and −0.011°C m^{-1}. We correct the VLR with an annual correction factor to preserve the seasonal patterns in the VLR.

3.3.3. Discharge Calibration

As the final calibration step, the parameters related to rainfall-runoff processes (Soilfactor, Rootdepth, crop coefficient multiplier, baseflow recession coefficient, ground water recharge delay time, and routing recession coefficient) are calibrated (supplementary Table S1). The model is calibrated against observed discharge at a daily time step for the locations where the discharge data is available (Table 1). In the BRA river basin (at Nu Xia), there were only 4 years (1979–1982) of discharge data; the model is calibrated for those 4 years and independently validated at Wangdirapids for a different period (2004–2008). In the GAN river basin, we calibrated and validated the model at Chisapani and independently validated it at Devghat. Similarly, in the IND river basin, we calibrated and validated model at the inflow of Tarbela dam and independently validated it at Dainyor bridge. The rainfall-runoff parameters were calibrated for each individual basin as shown in Table 1.

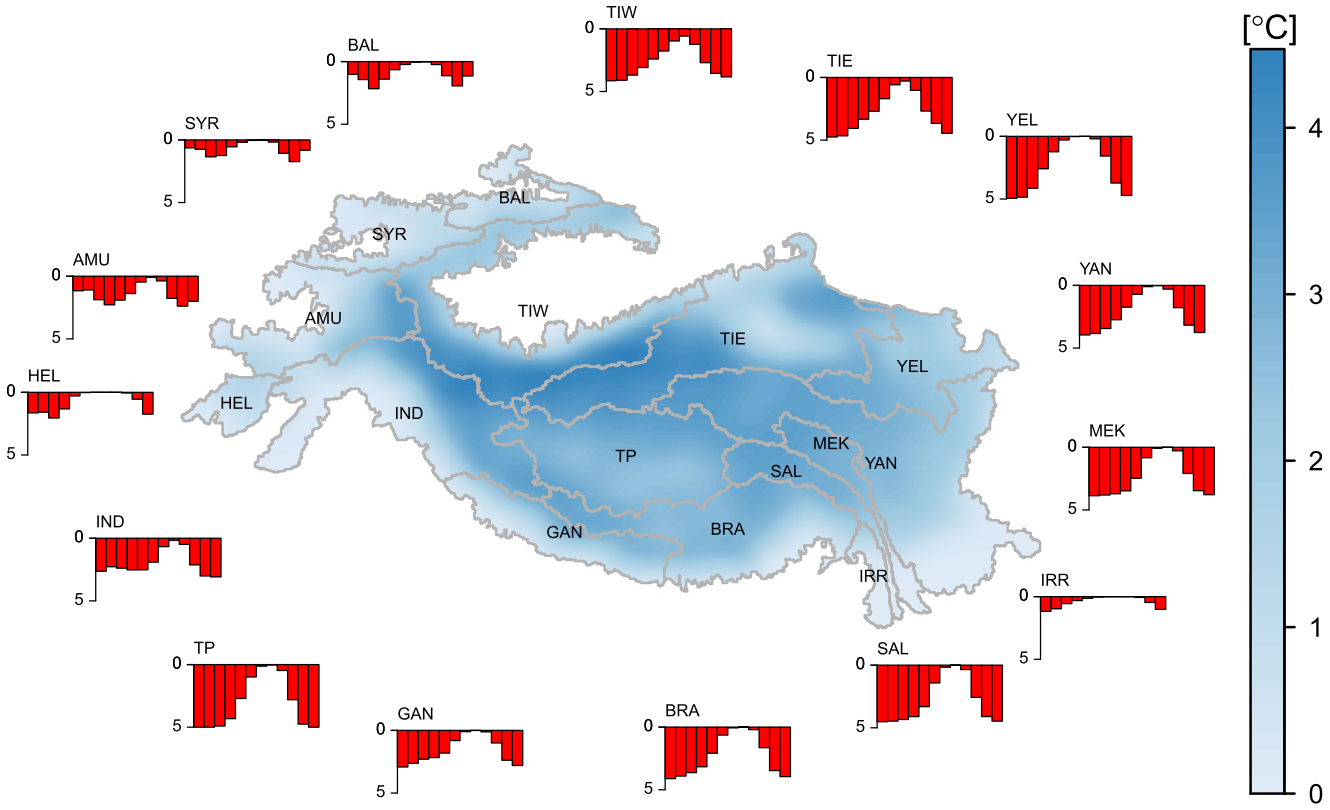

Figure 3. Basin averaged temperature bias-correction values (°C). The bars (red) represent the monthly temperature correction applied to each basin. The base map represents the annual averaged correction for the entire High Mountain Asia.

4. Results

4.1. Bias Correction

The bias correction results show high variability, among the basins in HMA (Figure 3). For instance, there are differences in the monthly variation and absolute values between the western and eastern parts. The basin averaged biases reflect significant seasonal variability in the basin as the correction is highest in winter and lowest in the summer season. The higher altitude areas show higher bias correction as compared to the lower altitude areas. The higher biases are found in the winter months, in particular for the higher altitude regions, where the temperatures are below 0°C (supplementary Figure S3). The seasonal and spatial variability in bias can be mainly attributed to the spatio-temporal variability of temperature in the basins (supplementary Figure S3). The interior river basins TIW, TIE, and TP show higher monthly corrections as compared to the other river basins in HMA. The IRR and HEL river basins have low average bias correction among all the other basins in HMA. In general, the southern (GAN and BRA) and eastern basins (MEK, SAL, YAN, and YEL) show higher correction as compared to the westerly dominated river basins (IND, HEL, AMU, SYR, and BAL). The seasonal variability of bias correction factors (higher for winter months and lower for summer months) from this study are in line with those based on the average of 33 observed meteorological stations (Orsolini et al., 2019). Thus, we conclude that bias corrected results of this study are realistic and satisfactory for use in further analysis.

4.2. Model Calibration and Validation

4.2.1. Calibration to Observed Snow Cover

The snow persistence calibration results also show a large spatial and seasonal variability. For instance, there is less variability for western basins compared to eastern parts (Figure 4). While SPHY overestimates snow persistence for the winter and spring seasons, the summer snow persistence is underestimated. The eastern

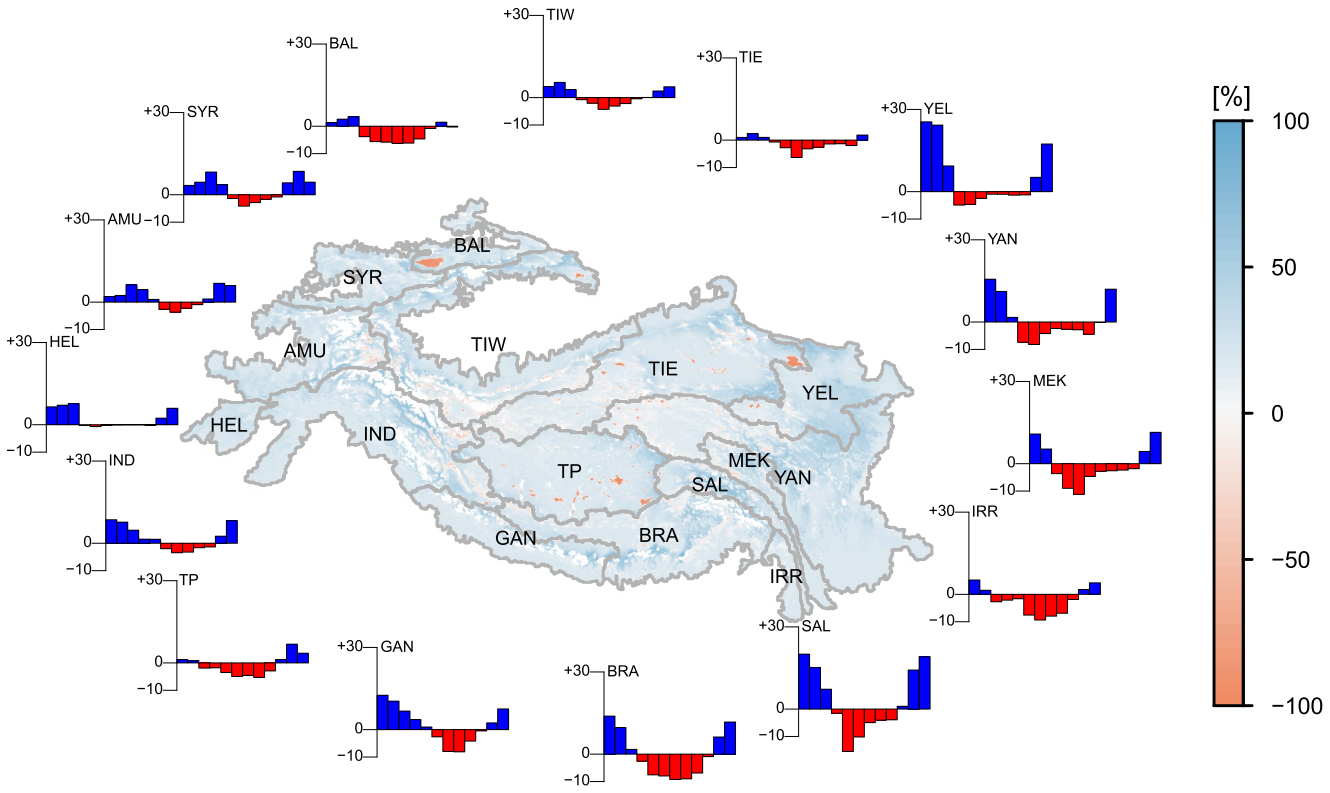

Figure 4. Difference in simulated and observed snow persistence between Spatial Processes in Hydrology (SPHY) and MODIS for 2001–2017. The bars represent the monthly average differences in snow persistence for each basin after calibration. The blue (red) bar indicates SPHY overestimating (underestimating) the MODIS snow persistence. The base map represents the annual difference in snow persistence for the entire High Mountain Asia.

Table 2
Simulated and Observed Glacier Mass Balance Aggregated to the Entire Upstream Basin After Calibration of Glacier Melt Parameters

Basin	Simulated (Gt yr^{-1})	Observed (Gt yr^{-1})
AMU	−1.12	−1.02
BRA	−4.44	−5.08
GAN	−2.13	−2.62
IND	−3.02	−3.92
IRR	0.00	−0.03
BAL	−0.54	−0.91
MEK	−0.11	−0.08
TP	−0.36	−0.47
SAL	−0.62	−0.75
SYR	−0.36	−0.38
TIE	−0.38	−0.19
TIW	2.14	0.15
YAN	−0.30	−0.40

Abbreviations: AMU, Amu Darya; BAL, Balkash; BRA, Brahmaputra; GAN, Ganges; IND, Indus; IRR, Irrawaddy; MEK, Mekong; TP, Plateau of Tibet Interior; SAL, Salween; SYR, Syr Darya; TIE, Tarim interior east; TIW, Tarim interior west; YAN, Yangtze.

(MEK, SAL, YEL, and YAN) and southern (GAN, BRA) river basins show higher variability as compared to the western (IND, HEL, AMU, SYR, and BAL) and interior river basins (TP, TIE, and TIW). The western and interior river basin snow persistence values are within the threshold of ±10% whereas eastern and southern river basins show higher overestimation. However, higher overestimation is only seen for the winter months in these basins. The overestimation of snow cover in winter months could be attributed to either the presence of cold biases in the ERA5 (even after the bias correction), too little sublimation or due to omission of other transport mechanism such as avalanching and snow redistribution by wind in the SPHY model which could eventually result in excessive snow accumulation and higher simulated snow cover. Overestimation of snow cover extent could potentially lead to an overestimation of snow runoff calculation. Given the scarcity of the snow related data in HMA, snow redistribution, avalanching or a physically explicit modeling of sublimation is computationally impossible. Moreover, the actual snow melt calculation depends on the snow water equivalent (SWE), which depends on snowfall. Though, there are spatial differences between observed and modeled snow cover, at basin scale this effect will be less pronounced.

4.2.2. Calibration to Observed Glacier Mass Balance

The glacier parameter calibration results are presented in Table 2. In general, the simulated mass balance after model calibration is in close agreement with the geodetic mass balance observations reported by Brun et al. (2017). However, for some river basins, the aggregated SPHY

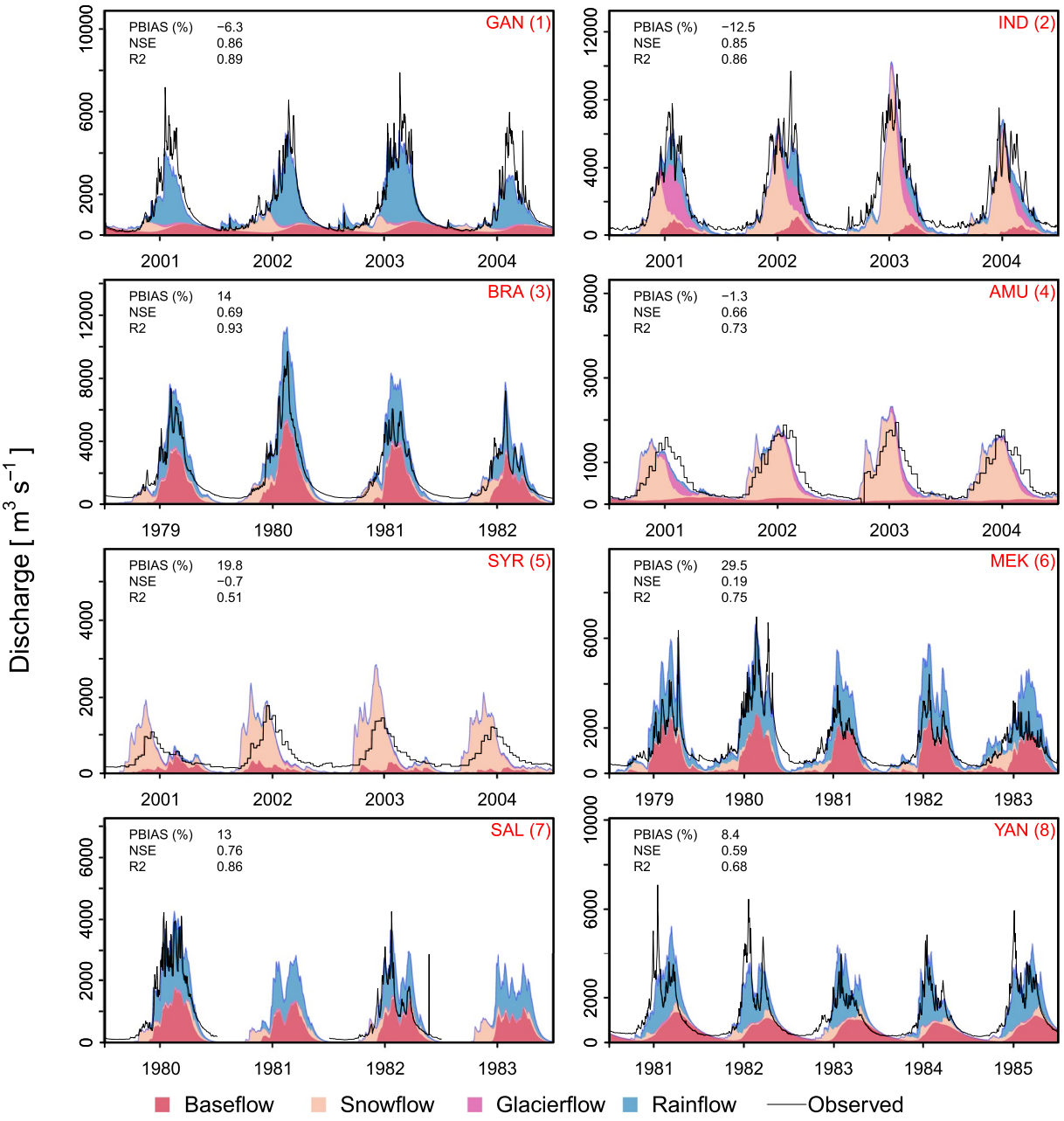

Figure 5. Observed and simulated discharge with the distinction of flow components at calibration locations shown in Figure 1 and Table 1 for the calibration time period. Each panel shows values for model performance indicators; Nash-Sutcliffe efficiency criterion (NSE), percent bias (PBIAS), and coefficient of determination (R^2) at the top left corner.

simulated glacier mass balance is too negative (TIE) or too positive (IND, BAL, and TIW). The underestimation in glacier mass balance can be attributed to lower snow degree-day factors and cold biases in ERA5 temperature. The lower temperature over the glacier surface results in the accumulation of seasonal snow in the winter and thus delays the glacier ice melt process.

4.2.3. Calibration to Observed Discharge

To estimate the efficiency of the calibration to discharge, we use the Nash-Sutcliffe efficiency criterion (NSE), percent bias (PBIAS), and coefficient of determination (R^2) as performance indicators (Nash & Sutcliffe, 1970). The daily NSE for the calibration period in the GAN, IND, BRA, AMU, SAL, and YAN river basins are 0.86, 0.85, 0.69, 0.66, 0.76, and 0.59 (Figure 5). The discharge calibration performance in most of

those basins is "very good" and in others, it is "satisfactory" (Moriasi et al., 2007). However, there is a large overestimation of the flow in the MEK (PBIAS = 29%) and SAL (PBIAS = 13%) river basins for the calibration period and even higher for the validation period. The overestimation in discharge can most likely be attributed to overestimation in precipitation amounts in ERA5 over these basins. A similar overestimation of precipitation in ERA5, leading to higher biases in simulated discharge, has been reported in several other studies (Cucchi et al., 2020; Harrigan, 2020). The overestimation of precipitation can be related to the spatial distribution and the sparse density of meteorological stations in HMA used for the ERA5 reanalysis (Jiang et al., 2020). Further, extremely large rainfall totals, to some extent, can be attributed to "rain bombs" in the numerical weather prediction model (NWP) used in ERA5 (Harrigan, 2020). Similarly, studies have reported large biases (PBIAS) up to 44% in ERA5 precipitation compared to ground-based observations in the Pamir region (Zandler et al., 2019). Moreover, overestimation of discharge for the calibration period (PBIAS = 19.6%, Figure 5) and validation period (PBIAS = 19.8%, supplementary Figure S4) in the SYR river basin are likely due to the precipitation overestimates of ERA5. The discharge simulations in westerly dominated and monsoon-dominated basins show different responses to the overestimation of precipitation. In the MEK and SAL river basins, which are monsoon dominated catchments, the overestimation of precipitation in the monsoon season causes quick overland flow, which leads to the large overestimation of discharge mainly in the monsoon season. However, in the westerly dominated SYR river basin, the dominant winter precipitation leads to the storage of solid precipitation in the snowpack. The overestimation of winter precipitation in ERA5 leads to excessive snowmelt in spring and the summer season. Furthermore, the coarse spatial resolution (5 × 5 km) and a simple routing scheme might also contribute to the overestimation of the simulated flow.

Additionally, the contributions of snow melt, glacier melt, rainfall-runoff and baseflow to overall discharge were compared to several other smaller-scale studies in the region (supplementary Table S2). For the Hunza subbasin at Dainyor, Mukhopadhyay and Khan (2014) analyzed annual hydrographs and reported a combined 74% of snow and glacier melt contribution to the total discharge, compared to our estimates of 86%. Shrestha et al. (2015) used WEB-DHM-S, a distributed biosphere hydrological model, and estimated 33% glacier melt and 49% snow melt contribution (average of 3 years 2001–2003), compared to our estimates of 37.4% and 48.7% for glacier and snow melt, respectively. Wijngaard et al. (2017) used a 5 × 5 km resolution SPHY hydrological model with a dynamic glacier mask for Hunza at Dainyor and reported a glacier and snow melt contribution of 18% and 69%, respectively. Similarly, Lutz et al. (2014) used a 1 × 1 km resolution SPHY hydrological model with a static glacier module and estimated largely different results, 81% and 10% from glacier and snow melt, respectively. This discrepancy can be largely attributed to their choice of a static glacier boundary which does not differentiate between glacier melt, snow melt and rainfall-runoff from glaciers, but defines all runoff from glacier areas as glacier melt. The dynamic glacier module in our study updates glacier boundaries at the end of the accumulation season every year.

The runoff contribution estimates from Wijngaard et al. (2017) for the Ganges basin at Devghat comprise 3.4% for glacier melt (compared to 4.1% for this study), 12.4% (9%) for snow melt, 63.4% (65.9%) for rainfall-runoff and 20.8% (21.0%) for baseflow, which are all in close agreement with values reported in this study. A similar close agreement in runoff partitioning was reported for the Brahmaputra catchment at Wangdirapids. Given the differences in scale, time period, modeling approach and input data, the runoff contribution estimates align well with past studies in this region. Considering the close agreement of runoff contributions compared to past studies, uncertainties in the ERA5 input data and the large spatial model domain, we conclude the model performance is satisfactory for our purpose.

Either limited or no discharge data availability for the hydrological model calibration is a key issue in the data scarce HMA region. Due to the lack of available discharge data for other basins, we adopt a "vector teams" approach to transfer the parameters for the ungauged basins (Bárdossy, 2007). The basins adjacent to each other with similar climatic and physiographic characteristics tend to hydrologically behave in a similar manner (Merz & Blöschl, 2004; Patil & Stieglitz, 2014). We transfer the parameter sets between them as this approach has been widely used in several sub-basin, basin, and regional scale studies in the HMA region (Lutz et al., 2014, 2016; Nepal et al., 2017; Wijngaard et al., 2017). We transfer the rainfall-runoff parameters from the BRA to TP, SAL to IRR, YAN to YEL, and TIE, IND to TIW, and AMU to HEL and BAL river basins. Further, we validate the plausibility of transferred parameters by analyzing the patterns of annual and sea-

sonal variability in discharge reported in the public domain for those basins. Finally, we conclude that the parameter transfer approach from a gauged basin to neighboring ungauged basins in HMA is applicable.

4.3. Hydrological Regimes

The climate in the western mountain ranges (Karakoram, Hindu Kush, Pamir, and parts of Tien Shan and Kunlun) is primarily influenced by westerly disturbances and characterized by large amounts of snowfall in the winter season (Figure 2). This snow melts and contributes to the river flow in the spring and summer in the AMU, SYR, HEL, BAL, and IND river basins (Figure 1). A considerable amount of precipitation falls as snow (% of annual precipitation) in the AMU (45%), SYR (29%), HEL (30%), IND (35%), and BAL (24%) basins (supplementary Table S3). These basins are also characterized by vast glacierised areas, particularly in the IND (6.3% of total upper basin area). Therefore, the hydrology in these basins is dominated by snow and glacier melt (Figure 6). The total melt contribution to runoff, from snow and glaciers, in the AMU (79%), SYR (74%), HEL (78%), and IND (45%) is higher than in other river basins (Table 3).

In contrast, the hydroclimate in the southern and south-eastern basins is dominated by the Indian monsoon. Most of the annual precipitation falls during the summer monsoon months (June, July, August, and September) in the GAN (71%), BRA (60%), IRR (62%), MEK (66%), and SAL (63%) basins (supplementary Table S3). The hydrology in these Himalayan rivers is dominated by the rainfall-runoff component (Figure 1). A large amount of monsoonal precipitation over the GAN river basin explains the relatively small melt contribution (13%) despite having a relatively large area covered by glaciers (4.4%). A similar rainfall-runoff dominated regime can be observed in the wet eastern HMA in the YAN (71%) and YEL (64%) river basins. In these eastern river basins, the melt contribution is small due to the small glacier area coverage (0.4% and 0.1%, respectively) and little precipitation falling as snow (7% and 11%). The endorheic basins on the interior of the Tibetan Plateau (TP) show a stronger monsoonal precipitation pattern than other river basins in the Himalayan arc. The spring, autumn, and winter seasons are very dry, and 80% of the annual precipitation falls during the monsoon period (Bookhagen & Burbank, 2010). Even though the average elevation of the TP is above 4,500 m, only 12% of annual precipitation falls as snow in the region, since most precipitation falls during summer when T is above 0°C (Figures 1 and 2), even at this a high altitude. Consequently, a rainfall-runoff regime, with 89% of the total annual flow occurring during the monsoon, is prevalent in the region. The northern basins, TIW and TIE, surrounded by the Pamir in the West, Karakoram in the South-East, Kunlun Shan in the East, and Tien Shan in the North are among the driest basins in the entire HMA. These basins have a continental climate with high evapotranspiration rates (35% and 41% of annual precipitation) in the central dry region and high sublimation (17% and 18% of annual precipitation) on the surrounding mountain parts. The higher melt contribution to the runoff in the TIW (34%) as compared to TIE (21%) can be explained by the relatively larger glacierised area (5.8%) in TIW as compared to TIE (0.9%).

We define four different (single and mixed) hydrological regimes based on the dominant contributors: Nival (N; snowmelt dominated), Pluvial (Pl; rainfall-runoff dominated), Glacial-Nival (GN; snow and glacier melt dominated), and Nival-Pluvial (NP; snowmelt and rainfall-runoff dominated). We use three different thresholds for the snowmelt (15%), glacier melt (3%), and rainfall-runoff (40%) contribution to categorize the regimes. The baseflow contribution is excluded from hydrological regime distinction. The runoff contributions for each basin (Table 3) are recalculated excluding baseflow contribution. If two or more threshold criteria are exceeded, then it is considered as a mixed hydrological regime. We find five basins with a nival-glacial regime (AMU, GAN, IND, BAL, and TIW), six basins with a nival-pluvial regime (BRA, MEK, TP, SAL, TIE, and YEL), two basins with a nival regime (HEL and SYR) and two basins with a pluvial regime (IRR and YAN). These thresholds were selected to ensure the basins with a large fraction of glacier areas compared to upstream basin area (e.g., IND, TIW, and AMU) stand out with a nival-glacial regime. For some basins, in particular BRA, even though the glacier area is greater than 10,000 km^2, the overall contribution of glacier melt was less than 3% and thus was not included in nival-glacial regime. The thresholds selected were subjective to the upstream basin boundaries used in this study.

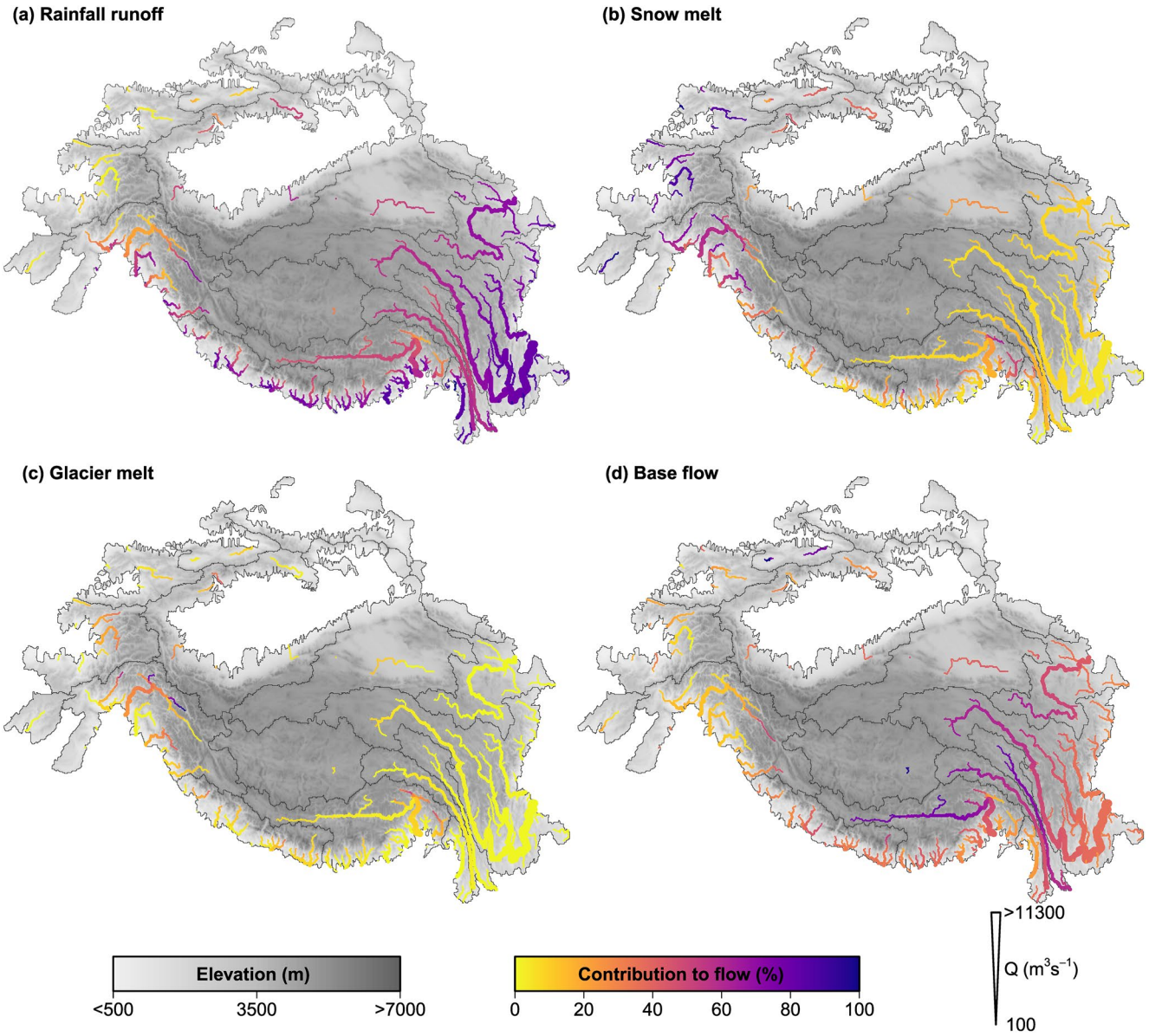

Figure 6. Flow components of the average annual total runoff for the reference ERA5 period (1985–2014). The magnitude of total annual flow is represented by the thickness of the line, color indicates the relative contribution to the total annual flow.

4.4. Hydrological Responses at Different Time Scales

4.4.1. Seasonal Shifts in Flow Peaks

Here, we investigate the shifts in peak timing, and magnitude changes in basin aggregated total runoff between the EOC and the reference period for the four different hydrological regimes. The increasing fraction of liquid precipitation attributed to climate warming results in a faster translation of precipitation to runoff and results in a higher magnitude of peak runoff in all the basins. Four out of 15 basins show a clear shift in peak flow timing of total runoff. Basins with GN hydrological regimes, in particular the AMU, IND, and BAL basins, show changes in the total runoff patterns for the EOC period (Figure 7). For these basins, the onset of snow (supplementary Figure S5) and glacier melt runoff (supplementary Figure S6) starts earlier in the spring season in the EOC period. This results in an earlier peak flow as compared to the reference period. In the AMU basin, the peak of total runoff is shifted from June in the reference period to April for the EOC warm-wet, warm-dry, and cold-dry and to May for the cold-wet scenario. A significant increase in peak

Table 3
Basin Characteristics for the Reference Period (1985–2014)

Basin	Precipitation (mm yr^{-1})	Area (Km^2)	Glacier Area (%)	Runoff (mm yr^{-1})	Runoff coef. –	CV of runoff (%)	% Contribution to total runoff: Glacier Melt	Snow Melt	Rainfall Runoff	Base Flow	Melt (%)
Amu Darya (AMU)	676	268,280	4.36	407	0.60	89	4.4	74.4	5.4	15.8	78.8
Brahmaputra (BRA)	2,018	400,182	2.73	1,575	0.78	85	1.8	13.2	62.1	22.8	15.0
Ganges (GAN)	1,763	202,420	4.37	1,293	0.73	101	3.1	10.3	64.7	22.0	13.4
Helmand (HEL)	360	74,334	0.00	195	0.54	140	0.0	77.5	5.2	17.4	77.5
Indus Basin (IND)	832	473,494	6.28	577	0.70	83	5.1	39.7	43.9	11.4	44.7
Irrawaddy (IRR)	3,638	49,029	0.15	3,223	0.88	87	0.0	5.1	78.2	16.7	5.1
Lake Balkash (BAL)	856	121,185	3.39	543	0.62	43	2.2	46.3	9.3	42.3	48.5
Mekong (MEK)	1,066	110,678	0.26	528	0.49	101	0.3	7.4	55.1	37.2	7.7
Plateau of Tibet Interior (TP)	451	415,197	0.83	117	0.25	162	2.3	15.3	32.8	49.6	17.6
Salween (SAL)	1,091	119,377	1.45	627	0.57	94	1.4	14.7	55.7	28.3	16.1
Syr Darya (SYR)	942	172,704	1.70	456	0.48	97	1.3	72.9	5.6	20.2	74.2
Tarim Interior East (TIE)	305	600,182	0.90	126	0.42	93	1.1	20.2	49.7	29.0	21.3
Tarim Interior West (TIW)	373	481,481	5.77	166	0.45	103	5.8	28.4	44.4	21.4	34.2
Yangtze (YAN)	1,127	687,150	0.39	849	0.75	76	0.2	5.5	71.0	23.3	5.7
Yellow (YEL)	751	272,857	0.05	468	0.62	77	0.1	9.6	63.9	26.5	9.6

The basin represents the upstream catchment area, as shown in Figure 1. Acronym CV represents the coefficient of variation.
Abbreviations: AMU, Amu Darya; BAL, Balkash; BRA, Brahmaputra; GAN, Ganges; HEL, Helmand; IND, Indus; IRR, Irrawaddy; MEK, Mekong; TP, Plateau of Tibet Interior; SAL, Salween; SYR, Syr Darya; TIE, Tarim interior east; TIW, Tarim interior west; YAN, Yangtze; YEL, Yellow.

total runoff is also projected for the AMU basin in the future. Although all runoff components contribute to the peak total runoff, the snowmelt runoff contribution dominates, compared to the glacier and rain-runoff (supplementary Figures S5, S6, and S7). An early total runoff peak that is mainly due to snow and glacier melt, as observed for the IND basin, is also observed in the BAL basin for future scenarios. While the IND basin shows no changes in the timing of peak total runoff, interestingly, a bimodal hydrograph is observed for the future period. The first peak is mainly attributed to the early snow and glacier melt while the second peak is primarily due to the rainfall-runoff during the monsoon. In contrast, the peak of total runoff in the TIW basin is shifted to later in the year (July) as compared to the reference period (June). This is predominantly due to the earlier onset of melt and removal of seasonal snow from the ice surface, resulting in rapid glacier ice melt in combination with increased monsoon precipitation in the future.

Among other basins with a GN hydrological regime, the GAN basin does not show changes in seasonality for total runoff in the future. Even though the snowmelt runoff in the GAN shows a clear shift to earlier onset of snowmelt in spring, like all basins in HMA, this effect is not reflected in the total runoff due to the dominant contribution of rainfall-runoff in the monsoon season. For the basins with an NP hydrological regime, there are no shifts observed in the timing of total runoff in future scenarios. Interestingly, for the BRA basin, a decrease in the hydrograph's rising limb slope is observed after a small peak in the total runoff in the months (MAM) for the future. This reduction in slope is mainly due to reduced snowfall resulting in a decrease in snowmelt contribution in future scenarios. A similar slope reduction is observed in all the basins with an NP hydrological regime. Basins with an N regime do not show specific changes in seasonality except the SYR for the warm-dry scenarios in the EOC period. The HEL and SYR basins initially show a significant increase in total runoff, mainly due to the rapid melting of seasonal snow in the early spring months and increased rainfall runoff contribution as compared to the reference conditions. Basins with a Pl regime do not show any significant changes in seasonality as most of the changes are associated with increases in rainfall-runoff during the monsoon season.

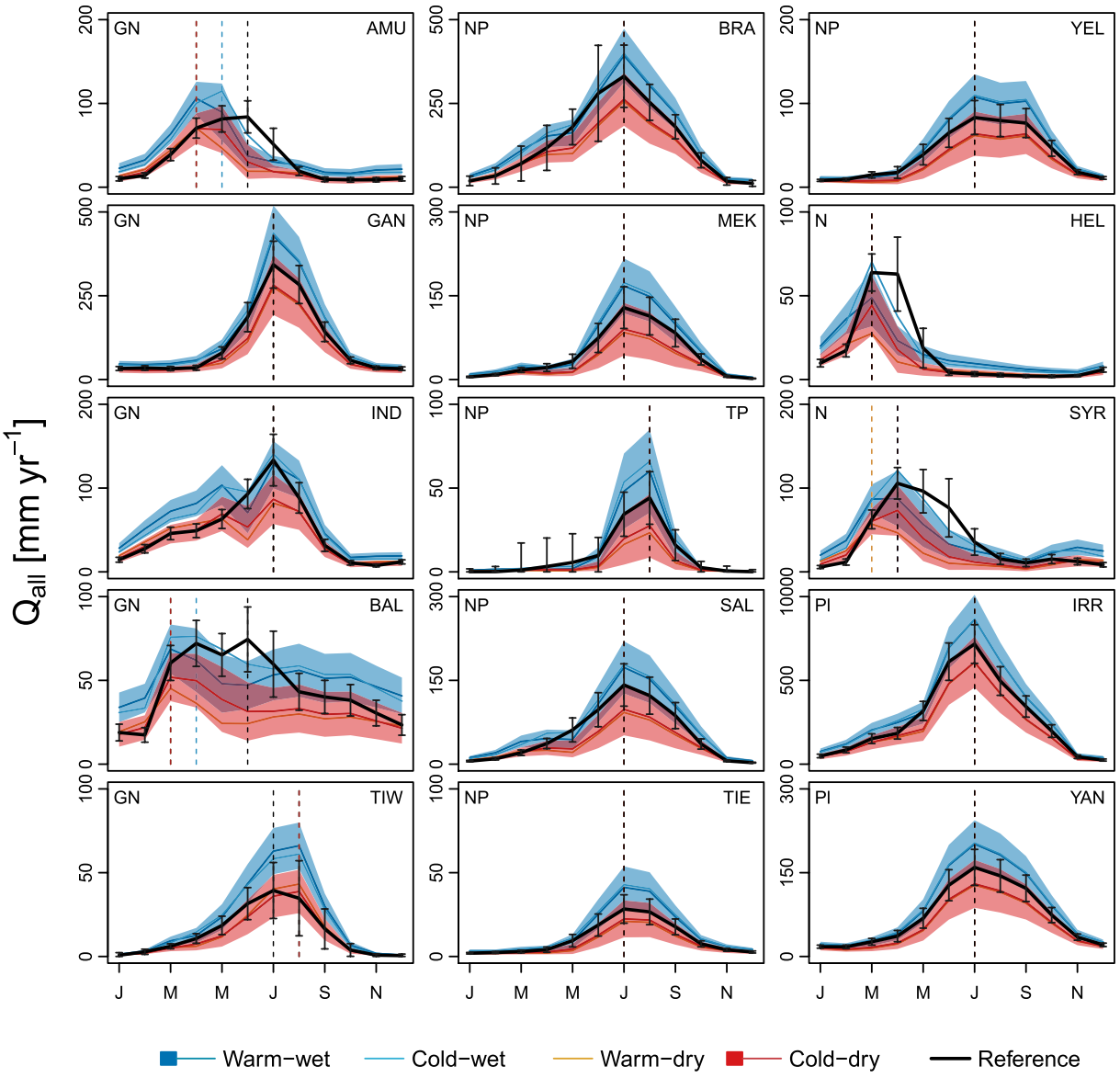

Figure 7. Changes in the mean annual cycles of total runoff by the end of the century (2071–2100) for the four hydrological regimes. The colored lines represent the mean of four groups of future scenarios, consisting of 12 dT/dP combinations each; warm-wet (6°C–8°C, 10%–40%), cold-wet (3°C–5°C, 10%–40%), warm-dry (6°C–8°C, −30%–0%), and cold-dry (3°C–5°C, −30%–0%). The color shadings represent ±2 standard deviation for a group of scenarios (only shown for warm-wet and cold-dry). The black solid lines represent the reference (1985–2014) mean annual cycle of total runoff. The vertical black error bar represents the total estimated variance calculated using first order second moment method for the reference climate for period 1985–2014. The vertical dashed lines represent the peak flow months for each group of scenarios. The text on the top-left and top-right gives the hydrological regime and basin name, respectively.

Although same future projections (dP and dT) were imposed, the response of individual runoff components (supplementary Figures S5–S7) and total water availability is different in magnitude and peak timing for basins across HMA (Table 4). The differences in total water availability are due to the combined effect of changes in individual runoff components. Climate change response on the overall water budget of a region is primarily driven by the climatic characteristics but also by physiographic characteristics, human interventions, and socioeconomic changes. The changes reported here represent the combined effect of climatic and physiographic changes related to snow and glacier processes.

A first-order second moment (FOSM) uncertainty analysis (see Supplementary Text S2 for details) suggests that uncertainty estimates for some basins (BAL, TIW, BRA, TP, HEL, and SYR) are higher than the others

Table 4
Relative Changes in the Magnitude (%) for Mean Annual Total Runoff for the Future End of Century Time Period (2071–2100) as Compared to the Reference Period (1985–2014)

	Warm-wet	Cold-wet	Warm-dry	Cold-dry
AMU	19.6 (14.4)	24.3 (14.6)	−27.2 (12.9)	−23.4 (13.2)
GAN	23.0 (13.4)	25.5 (13.4)	−22.4 (13.0)	−20.1 (13.1)
IND	29.7 (13.5)	28.4 (13.4)	−15.7 (12.9)	−16.6 (12.8)
BAL	10.3 (14.8)	19.9 (14.9)	−37.8 (13.5)	−29.1 (14.0)
TIW	58.0 (19.5)	50.9 (19.2)	−4.9 (17.0)	−11.3 (17.1)
BRA	18.2 (12.7)	21.0 (12.7)	−24.5 (12.2)	−22.0 (12.3)
MEK	26.4 (19.8)	32.4 (20.0)	−37.2 (17.0)	−32.5 (17.5)
TP	24.4 (28.0)	40.4 (29.7)	−53.2 (17.3)	−44.1 (19.6)
SAL	22.8 (17.6)	27.9 (17.8)	−34.9 (15.8)	−30.8 (16.2)
TIE	37.8 (21.3)	45.4 (21.5)	−29.6 (17.9)	−23.5 (18.5)
YEL	22.5 (15.6)	26.7 (15.7)	−29.7 (14.9)	−25.9 (15.1)
HEL	0.9 (15.2)	12.9 (15.7)	−46.8 (13.0)	−36.0 (13.7)
SYR	0.1 (16.6)	15.0 (17.6)	−49.0 (12.6)	−37.8 (14.0)
IRR	19.8 (11.4)	20.8 (11.4)	−19.7 (11.6)	−18.6 (11.6)
YAN	22.7 (13.4)	25.1 (13.4)	−23.2 (13.3)	−20.8 (13.4)

The values in the parentheses represent the standard deviation (±1).
Abbreviations: AMU, Amu Darya; BAL, Balkash; BRA, Brahmaputra; GAN, Ganges; HEL, Helmand; IND, Indus; IRR, Irrawaddy; MEK, Mekong; TP, Plateau of Tibet Interior; SAL, Salween; SYR, Syr Darya; TIE, Tarim interior east; TIW, Tarim interior west; YAN, Yangtze; YEL, Yellow.

(AMU, GAN, and IND) (Figure 7). To understand the underlying reasons for the variability in uncertainty estimates, the contribution of variance in individual parameters to the total variance is calculated (see Supplementary Figure S8). The uncertainty in meteorological forcing input (precipitation and temperature) is an order of magnitude higher compared to the model parameter uncertainty (DDFCI and DDFS). The precipitation uncertainty is highest in all basins, except for TIW and BRA, followed by uncertainty in T, DDFS, and DDFCI. The analysis suggests a large uncertainty in reference climate of the HMA region which limits the interpretation of climate change scenarios.

The seasonal shifts shown in Figure 7 represent the changes across several climatic combinations. Averaging the results in these broad categories, does not reveal the changes for the individual scenarios. Still, several clear trends of shifts in timing of the peak melt runoff, the overall change in contribution of runoff contributors are similar for basins with a similar hydrological regime. To illustrate changes at the seasonal scale for different time horizons, we take one basin from each of the hydrological regimes as an illustrative example: IND basin for GN, TP for NP, SYR for N, and YAN for Pl. We show these changes for the MC and EOC periods for the high dT, high dP, and high dPdT scenarios. For basins with a GN hydrological regime under the high dT scenario in both the MC and EOC periods, the seasonal changes are mainly driven by an initial increase in snowmelt runoff in the spring months followed by a decrease in snowmelt and an increase in glacier melt in the monsoon months (Figure 8 and supplementary Figure S9). The initial increase in snowmelt results from earlier melting of seasonal snow due to an increase in temperature. Moreover, an increase in temperature will further reduce the likelihood of precipitation falling as snow and intensifies the glacier ice melt process, thus increasing the glacier melt contribution. Clearly, the magnitude of change varies in the two future periods and is higher for the EOC than for the MC period. For the high dP scenario, changes are mainly driven by an increase in rainfall-runoff and snowmelt contribution, whereas for the high dPdT scenario, the changes are driven by an increase in rainfall-runoff, as well as snow and glacier melt contributions outside the monsoon season. A similar decrease of snowmelt runoff during the monsoon season is observed in the high dPdT scenario. For river basins with aN regime, changes in snowmelt contribution are mainly driving the changes in the future, for all three scenarios. These changes include a significant reduction of snowmelt contribution and shifts in peak melt water timing. While the changes in the future, for both time horizons and across all scenarios, are mainly driven by the snowmelt and rainfall-runoff contributors for river basins with aNP regime, rainfall-runoff drives the changes in river basins with a Pl regime, especially in the monsoon season. The scenarios with precipitation changes, that is, high dP and high dPdT, show a higher magnitude of rainfall-runoff change compared to high dT scenarios for basins with a Pl regime. The snow melt related changes are insignificant in the Pl regime compared to all other regimes where snow plays a dominant role in driving future changes. Thus, at the seasonal scale, changes are mainly driven by either change in snowmelt, rainfall-runoff, or a combination of both.

4.4.2. Changes in Decadal Time Scales for Runoff Contributors

In contrast to the high dP scenario, under the high dT scenario, a significant impact is observed for the snow and glacier melt contributions in river basins with a GN regime, at yearly to decadal scales (Figure 8). Glacier melt in the basins with a GN regime shows a slower melting response and smaller changes for the high dP scenario as compared to the high dT scenario. Moreover, the glacier melt contribution for basins with a GN regime shows an initial increase and the peak of glacier melt is reached by the end of the MC period, which is then followed by a strong decline by the start of the EOC period. The initial increase results from warming induced melt, which eventually is offset by a reduction in available ice volume. In particular, smaller glaciers will reach the glacier melt peak in the next few decades or by the MC period, followed by

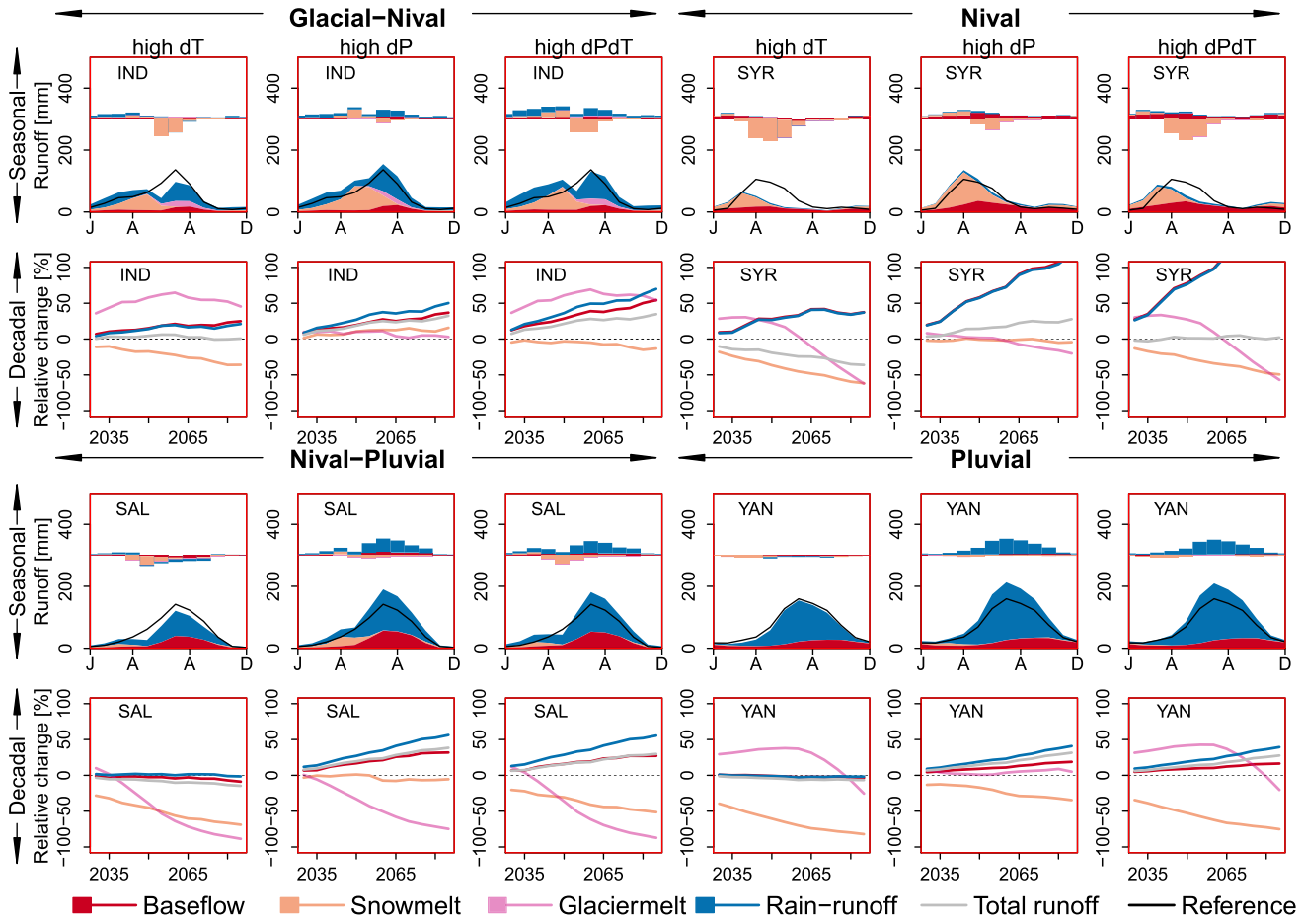

Figure 8. Hydrological response to climate change at seasonal (row 1 and 3) and decadal time scales (row 2 and 4). The seasonal hydrographs and changes in flow components (bars) are plotted for the end of century period (2071–2100) for one illustrative basin from each hydrological regime, that is, Glacial-Nival (IND), Nival-Pluvial (SAL), Nival (SYR), and Pluvial (YAN). Changes in the flow regime are assessed for three different future scenarios, that is, high dT, high dP, and high dPdT. The bars in seasonal plots represent changes per-flow component relative to the reference period (1985–2014). The black solid lines in seasonal plots represent the reference mean annual cycle of total runoff. The lines in decadal plots represent the transient 30-year running mean relative changes in annual sums of rainfall-runoff, glacier melt, snowmelt, baseflow and total runoff. The 30 years mean is calculated at 5-year intervals.

a permanent loss in glaciated area except for the TIW where glacier melt has not reached its peak melt by the EOC and contributes strongly to the peak total runoff (supplementary Figure S10). Interestingly, the increases in glacier melt runoff, rainfall-runoff, and baseflow contributions are offset by a significant decrease in snowmelt contribution in river basins with a GN regime. This results in almost no change in the total runoff for the high dT scenario. While the glacier melt keeps increasing by the EOC period in river basins with a GN regime, the initial increase eventually starts decreasing by the MC or EOC periods for basins with other hydrological regimes. An explanation is that most of the basins have either passed or are approaching the peak in glacier melt runoff. For all the regimes, the high dP scenario leads to an increase in rainfall-runoff and baseflow contribution, which leads to a consistent increase in total runoff in the future. On the other hand, the high dPdT scenario shows a nonlinear response on the longer time scales when compared to either the high dP or high dT scenarios for all the regimes. In the high dPdT scenario, a significant increase in the rainfall-runoff and baseflow contributions is observed across regimes. An increase in liquid P as a result of high T and an increase in precipitation are the main factors causing the increase in rainfall-runoff and baseflow. The high dPdT scenario results in an increased total runoff in all regimes except the N regime as the increase in rainfall-runoff is offset by the decrease in glacier and snowmelt runoff.

5. Discussion

5.1. Climate Change Response at Smaller Spatial Scales

The climate change response of hydrological processes explored here is highly scale dependent. It varies both spatially from catchment to basin-scale and temporally from the seasonal to the decadal scale. The responses vary strongly in the climatically and hydrologically diverse HMA region, where runoff generated at higher altitude depends strongly on snow and glacier melt, whereas rainfall-runoff and baseflow processes dominate runoff generation at lower altitudes. In HMA, the changes in total water availability are larger at higher altitudes than at lower altitudes for the different hydrological regimes except in the HEL and MEK basins (Figure 9). Even though the scenarios show similar patterns, the magnitude differs. Magnitudes are higher for the warm-wet and cold-wet scenarios as compared to the warm-dry and cold-dry scenarios. For higher altitudes, the total water availability increases either due to increased melt or an increase in the liquid precipitation fraction. Both conditions are mainly driven by increased temperature or precipitation. The differences in the magnitude of flow components and total water availability for high altitude regions are well visible in two extreme scenarios; warm-wet (supplementary Figure S11) and cold-dry scenarios (supplementary Figure S12). However, this increased water availability levels off and decreases when lower altitude regions are considered as well. The TIW and TIE show the strongest changes for the higher altitudes among all the basins in HMA. This is mainly due to the increase in future total water availability driven by a stronger increase in monsoon precipitation (supplementary Figure S7) and glacier melt (supplementary Figure S10) in those basins.

Even though the total water availability at higher altitudes increases, the changes in timing and magnitude of peak water availability and seasonality impose a serious threat on the livelihood of people. In particular, agricultural productivity at high altitude regions which depend on the timing of melt from snow and glaciers are strongly exposed to cryospheric changes and will be impacted by future changes in hydrological regime and peak melt water availability for irrigation (Qin et al., 2020).

5.2. Hydrological Regimes at Smaller Spatial Scales

The characterization of hydrological regimes depends on the choice of thresholds of runoff contributors and the spatial aggregation level. To demonstrate this, we show the distinction of hydrological regimes differs for a varying spatial aggregation level. We compare hydrological regimes at three spatial aggregation levels: (a) river basins (i.e., the 15 upper basins), (b) subbasins as defined in the hydro-basins data set at aggregation level 06, and (c) subbasins as defined in the hydro-basins data set at aggregation level 08 (supplementary Figure S2). At each of these aggregation levels, we plot the contribution from rain, snow, and glacier melt runoff in a ternary plot (Figure 10). At the river basin aggregation level, the contribution from rain and snow dominates due to the substantial reduction in the relative contribution of glacier melt water with water from these sources (Figure 10a). Defining the hydrological regime based on the relative contributions of streamflow contributors will result mostly in rain or snow dominated flow regimes. However, the contribution changes with the finer spatial aggregation levels (Figure 10). For aggregation level 08, the glacier and snow contribution increases. For instance, the GAN river basin at basin aggregation level suggests a mostly rain dominant (80%) regime (Figure 10a). But at aggregation level 08, a higher number of subbasins have higher contribution from snow and glacier melt, despite the majority of subbasins being rain-dominated (Figure 10c). This highlights the importance of spatial scale in the distinction of hydrological regimes. In this study, we use basin and the relative contributions from rain-fall runoff, snow melt runoff, and glacier melt runoff at the river basin scale aggregation for the distinction of hydrological regime. The use of different thresholds and spatial scales would change the hydrological regime characterization and consequently the analysis.

5.3. Comparison with Other Studies

The differences in spatial and temporal aggregation, time horizons, models, and reference and future climate forcing make a comparison to other studies not straightforward. Even though the absolute magnitude of projected changes cannot be directly compared with studies that use inputs from either regional or global climate models, the patterns and direction of change are similar and comparable. The patterns of future

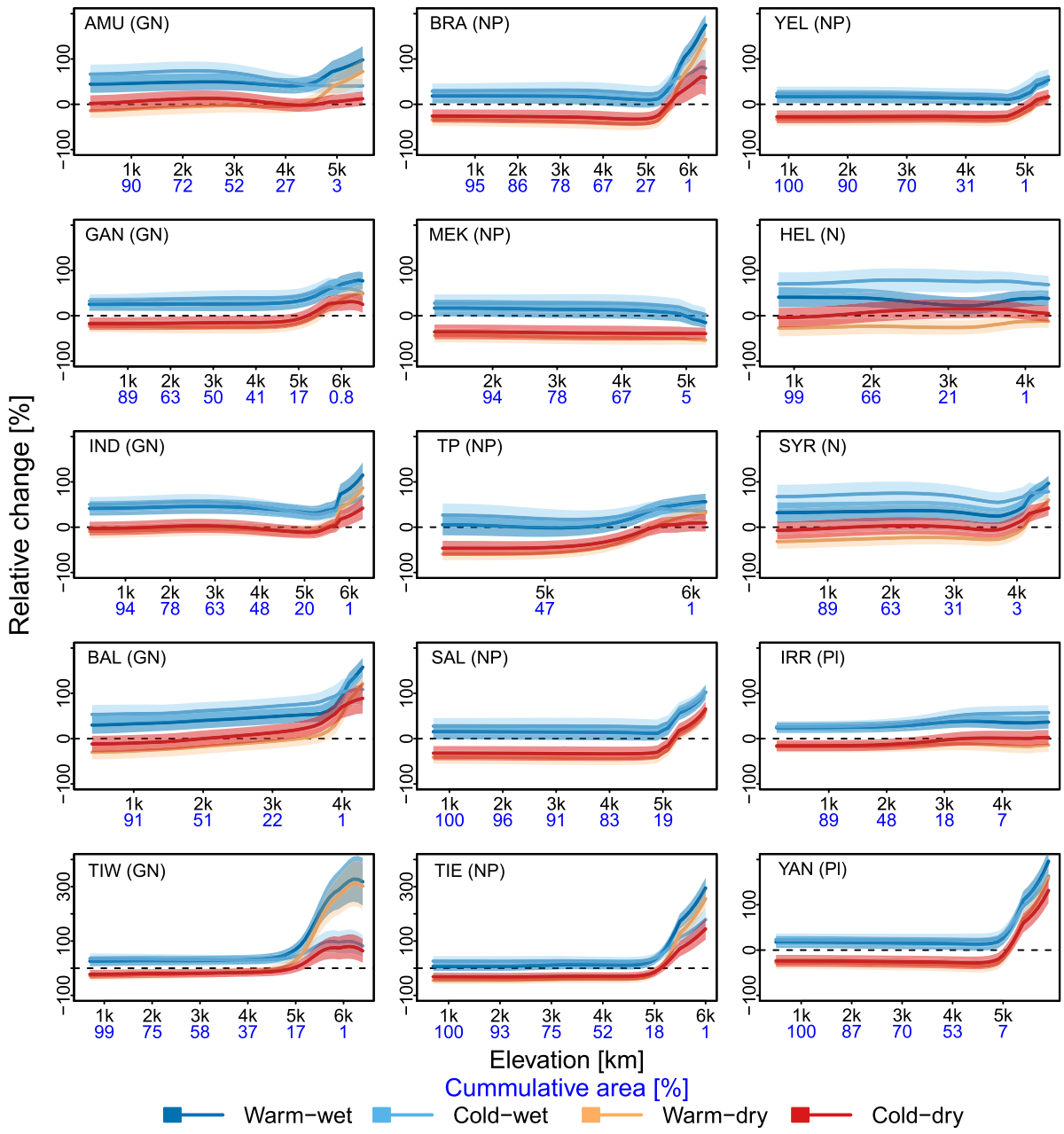

Figure 9. Relative changes in total runoff as a function of elevation by end of century (2071–2100). The black and blue *x*-axis labels represent the elevation [km] and cumulative area fraction above each 100 m elevation bin [%]. The color represents four future scenarios; warm-wet (6°C–8°C, 10%–40%), cold-wet (3°C–5°C, 10%–40%), warm-dry (6°C–8°C, −30%–0%), cold-dry (3°C–5°C, −30%–0%). The solid line indicates the mean of the model combination, and shading represents ±1 standard deviation (only shown for warm-wet and cold-dry). The text on the top right represents basin names with hydrological regimes in parentheses. Note the different scaling used for Tarim interior west and Tarim interior east.

change in seasonality and peak melt water in this study align with the other regional and global studies (e.g., Huss & Hock, 2018; Lutz et al., 2014; Wijngaard et al., 2017). Future increases in total water availability from this study (summarized in Table 4) are comparable to those reported at basin outlets by Wijngaard et al. (2017) for the similar future EOC period (i.e., 29%–41% for the GAN, 24%–49% for the BRA, and 4%–51% for the IND under RCP4.5 - RCP8.5). The total water availability for the BRA basin in this study is also comparable to the values reported by Lutz et al., (2014): −15%–60% for combined RCP4.5 and 8.5 emissions scenarios. The changes in seasonality and early melt dominated regimes found in this study are in line

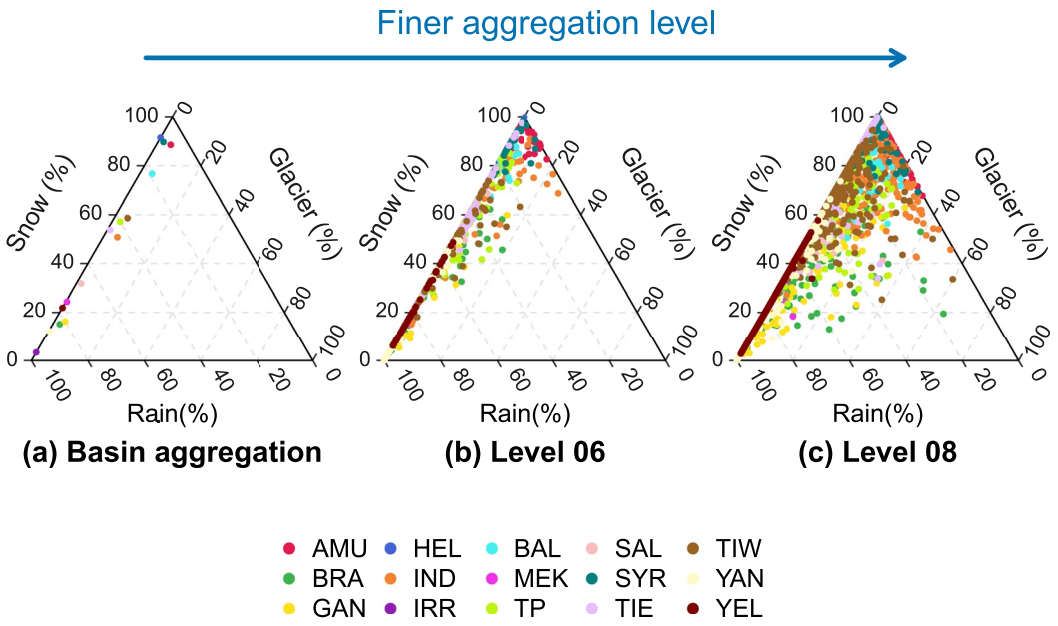

Figure 10. Ternary plot for hydrological regimes at the basin and hydro-basins (Lehner & Grill, 2013) aggregation levels 06 and 08. The axes give the different flow contribution (snow, glacier, and rainfall-runoff) to the total flow expressed in percentage [%]. The colored points represent the temporal aggregation for each spatial aggregation level.

with previous basin and sub-basin scale studies (Lutz et al., 2014; Ragettli et al., 2016; Sorg et al., 2014). The peak glacier melt timing found in this study are also consistent with the results of Huss and Hock (2018).

5.4. Uncertainties and Limitations

The results of this study heavily rely on the ERA5 reanalysis data and are therefore subject to limitations in those. In particular, the overestimation of precipitation in the monsoon dominated HMA regions results in overestimation of historical total water availability in those regions. However, the relative changes in future total water availability will not deviate significantly due to the historical overestimation. Computed changes in the absolute amount of glacier melt are also sensitive to the initial glacier states such as areas and ice volumes, which are subject to large uncertainties. The limited discharge data availability for the model calibration and parameter transfer approach is associated with uncertainties in the results. To reduce the uncertainty due to the parameter transfer approach, we use neighboring basins with similar climatic and physiographic characteristics in the approach and further validate the mean monthly climatological discharge values with those available in the public domain.

Furthermore, the range of projected changes in precipitation and temperature we use are based on a subset of 27 members of the CMIP6 model ensemble (Almazroui et al., 2020), and therefore may not cover the full range of uncertainty in future projections of the final CMIP6 ensemble. Nevertheless, the chosen ranges provide a good indication of the potential range of future changes. Moreover, the aggregated projected change over the entire region does not entirely resolve the micro-scale changes in the region where climate varies over short distances. Also, the use of a linear transformation of the historical climate to the future climate poses limitations. Seasonal variation in the climate change signals as well as non-uniform changes across the frequency distributions of temperature and precipitation are not considered, which may play a key role in future climate change response. Moreover, the uncertainty ranges for future runoff presented in this study represent the uncertainty from the range in future climate projections solely and do not include uncertainties in the input data and structural model uncertainty. Therefore, they represent the lower bound of uncertainty.

Apart from the improvement in simulation of physical processes, such as snow avalanching and sublimation, glacier melt and dynamics (debris, ponds, and cliffs), groundwater processes and flow routing, future

work must focus on developing a homogenized and representative climate data archive for HMA. More research is needed to improve the inadequacies and missing processes in the reference climatology, representation of key precipitation and temperature related processes in complex terrain like HMA. In-depth understanding of the full spread amongst CMIP6 models will be necessary to improve the interpretation of the highly space and time-dependent projections. Further, a more complex uncertainty analysis (e.g., a full Monte-Carlo or Bayesian approach) would be helpful to disentangle model input and structural uncertainty which is quite important for better interpretation of future climate change.

6. Conclusions

We show contrasting climate change responses across HMA's upstream river basins, dictated by the present-day variability in climate and hydrological regimes. At the large, river basin scale, the upstream basins of 15 rivers in HMA can be grouped into four hydrological regimes: glacial-nival, nival-pluvial, nival, and pluvial. Our results show that an increased fraction of liquid precipitation due to climatic warming results in higher peak total runoff in all the basins. Despite clear shifts at the seasonal scale in peak snowmelt runoff to earlier in the year in most cases, at the decadal to century scale only basins with glacial-nival hydrological regimes show shifts in the timing of peak runoff by the end of century. The snowmelt runoff decreases significantly for most of the basins toward the end of the century except for basins with a glacial-nival hydrological regime. This is found even for scenarios with moderate temperature increase. We demonstrate that all basins have either passed or are approaching the peak glacier melt runoff except the Tarim interior West basin, for which glacier melt continues to increase even by the end of the century. At the seasonal scale, the changes are mainly driven by changes in either snow or rainfall-runoff but at the decadal scale, the responses are rather consistent and mainly driven by precipitation changes. Finally, we illustrate that the changes in total water availability are stronger in magnitude for the headwaters than at lower altitudes. It is the change in seasonality and changes in peak melt runoff that will pose the main challenge to be addressed in adapting to future changes in a region where food security, energy security as well as biodiversity, and the livelihoods of many depend on water from the mountains. These findings provide important information to support climate change adaptation policy planning in this climate change hotspot.

Data Availability Statement

The ERA5 climate data are acquired from C3S Climate Data Store (https://cds.climate.copernicus.eu/cdsapp#!/dataset/reanalysis-era5-pressure-levels). The hydroBASINS data are obtained from HydroSHEDS repository (https://hydrosheds.org/page/hydrobasins). The authors acknowledge the World Climate Research Program for making the CMIP6 data set available for global and regional scale climate research (https://www.wcrp-climate.org/wgcm-cmip/wgcm-cmip6). The authors also thank the Earth System Grid Federation (ESGF) for archiving and providing access to the CMIP6 data set (https://esgf-node.llnl.gov/projects/cmip6/). The SPHY model codes can be accessed through the github repository (https://github.com/FutureWater/SPHY).

Acknowledgments
The project received funding from the Strategic Priority Research Program of Chinese Academy of Sciences, Grant No. XDA20100300. This project was also partly funded by the European Research Council (ERC) under the European Union's Horizon 2020 research and innovation programme (grant agreement number 676027 and 676819), and by the Netherlands Organization for Scientific Research under the Innovational Research Incentives Scheme VIDI (grant agreement 016.181.308). The authors thank Fanny Brun for providing the glacier mass balance data for high mountain Asia. The authors also thank the Nepal Department of Hydrology and Meteorology (DHM), the Pakistan Water and Power Development Authority (WAPDA), and the Bhutan National Center of Hydrology and Meteorology (NCHM) for providing discharge data. Streamflow data are also obtained from the Global Runoff Data Center (GRDC) (https://www.bafg.de/GRDC/EN/). We thank 3 anonymous reviewers for their constructive comments that helped to improve the manuscript. We would also like to thank Rene Wijngaard for helpful discussions.

References

Almazroui, M., Saeed, S., Saeed, F., Islam, M. N., & Ismail, M. (2020). Projections of precipitation and temperature over the South Asian countries in CMIP6. *Earth Systems and Environment*, *4*, 297–320. https://doi.org/10.1007/s41748-020-00157-7

Armstrong, R. L., Rittger, K., Brodzik, M. J., Racoviteanu, A., Barrett, A. P., Khalsa, S. S., et al. (2019). *Runoff from glacier ice and seasonal snow in High Asia : Separating melt water sources in river flow*, 1249–1261.

Ballesteros-Cánovas, J. A., Trappmann, D., Madrigal-González, J., Eckert, N., & Stoffel, M. (2018). Climate warming enhances snow avalanche risk in the Western Himalayas. *Proceedings of the National Academy of Sciences of the United States of America*, *115*(13), 3410–3415. https://doi.org/10.1073/pnas.1716913115

Bárdossy, A. (2007). Calibration of hydrological model parameters for ungauged catchments. *Hydrology and Earth System Sciences*, *11*(2), 703–710. https://doi.org/10.5194/hess-11-703-2007

Blöschl, G., Hall, J., Parajka, J., Perdigão, R. A. P., Merz, B., Arheimer, B., et al. (2017). Changing climate shifts timing of European floods. *Science*, *357*(6351), 588–590. https://doi.org/10.1126/science.aan2506

Böer, F. D. (2016). HiHydroSoil: A high resolution soil map of hydraulic properties (Version 1.2), Report 984. *Future Water*, *31*, 1–32. https://doi.org/10.1007/978-3-319-06540-3_21-1

Bolch, T., Kulkarni, A., Kääb, A., Huggel, C., Paul, F., Cogley, J. G., et al. (2012). The state and fate of himalayan glaciers. *Science*, *336*(6079), 310–314. https://doi.org/10.1126/science.1215828

Bookhagen, B., & Burbank, D. W. (2006). Topography, relief, and TRMM-derived rainfall variations along the Himalaya. *Geophysical Research Letters*, *33*(8), 1–5. https://doi.org/10.1029/2006GL026037

Bookhagen, B., & Burbank, D. W. (2010). Toward a complete Himalayan hydrological budget: Spatiotemporal distribution of snowmelt and rainfall and their impact on river discharge. *Journal of Geophysical Research*, *115*(3), 1–25. https://doi.org/10.1029/2009JF001426

Braithwaite, R. J. (2008). Temperature and precipitation climate at the equilibrium-line altitude of glaciers expressed by the degree-day factor for melting snow. *Journal of Glaciology*, *54*(186), 437–444. https://doi.org/10.3189/002214308785836968

Brun, F., Berthier, E., Wagnon, P., Kääb, A., & Treichler, D. (2017). A spatially resolved estimate of High Mountain Asia glacier mass balances from 2000 to 2016. *Nature Geoscience*, *10*, 668–673. [online] Available from. https://doi.org/10.1038/ngeo2999

Cannon, F., Carvalho, L. M. V., Jones, C., & Norris, J. (2016). Winter westerly disturbance dynamics and precipitation in the western Himalaya and Karakoram: A wave-tracking approach. *Theoretical and Applied Climatology*, *125*(1–2), 27–44. https://doi.org/10.1007/s00704-015-1489-8

Cao, B., Gruber, S., Zheng, D., & Li, X. (2020). *The ERA5-land soil-temperature bias in permafrost regions*, 1–22.

CAWater (2020). *CAWater Info: Portal of knowledge for water and environmental issues in Central Asia*. [online] Available from: http://www.cawater-info.net/index_e.htm Accessed 15 July 2020.

Cucchi, M., Weedon, G. P., Amici, A., Bellouin, N., Lange, S., Schmied, H. M., et al. (2020). WFDE5: Bias adjusted ERA5 reanalysis data for impact studies. *Earth System Science Data Discussions*, *12*(3), 1–32. https://doi.org/10.5194/essd-2020-28

Eyring, V., Bony, S., Meehl, G. A., Senior, C. A., Stevens, B., Stouffer, R. J., & Taylor, K. E. (2016). Overview of the Coupled Model Intercomparison Project Phase 6 (CMIP6) experimental design and organization. *Geoscientific Model Development*, *9*(5), 1937–1958. https://doi.org/10.5194/gmd-9-1937-2016

Farinotti, D., Huss, M., Fürst, J. J., Landmann, J., Machguth, H., Maussion, F., & Pandit, A. (2019). A consensus estimate for the ice thickness distribution of all glaciers on Earth. *Nature Geoscience*, *12*(3), 168–173. https://doi.org/10.1038/s41561-019-0300-3

Farr, T. G., Rosen, P. A., Caro, E., Crippen, R., Duren, R., Hensley, S., et al. (2007). The Shuttle Radar Topography Mission. *Reviews of Geophysics*, *45*(2). https://doi.org/10.1029/2005RG000183

Fu, P., & Rich, P. M. (1999). Design and implementation of the solar analyst: An ArcView extension for modeling solar radiation at landscape scales. *19th Annual ESRI User Conference*, 1–24.

Gardelle, J., Berthier, E., Arnaud, Y., & Kääb, A. (2013). Region-wide glacier mass balances over the Pamir-Karakoram-Himalaya during 1999–2011. *The Cryosphere*, *7*(4), 1263–1286. https://doi.org/10.5194/tc-7-1263-2013

GRDC. (2020). *BfG - The GRDC - Global Runoff Database*. [online] Available from: https://www.bafg.de/GRDC/EN/01_GRDC/13_dtbse/database_node.html Accessed 11 September 2020.

Hall, D. K., & Riggs, G. A. (2015). *MODIS/Terra snow cover monthly L3 global 0.05Deg CMG dataset version 6*. https://nsidc.org/data/MOD10CM

Hall, J., Arheimer, B., Borga, M., Brázdil, R., Claps, P., Kiss, A., et al. (2014). Understanding flood regime changes in Europe: A state-of-the-art assessment. *Hydrology and Earth System Sciences*, *18*(7), 2735–2772. https://doi.org/10.5194/hess-18-2735-2014

Hargreaves, G., & Samani, Z. (1985). Reference crop evapotranspiration from temperature. *Applied Engineering in Agriculture*, *1*(2), 96–99. https://doi.org/10.13031/2013.26773

Harrigan, S. (2020). *DRAFT - GloFAS-ERA5 operational global river discharge reanalysis*, 1–23.

Hersbach, H., Bell, B., Berrisford, P., Hirahara, S., Horányi, A., Muñoz-Sabater, J., et al. (2020). The ERA5 global reanalysis. *Quarterly Journal of the Royal Meteorological Society*, *146*(730), 1999–2049. https://doi.org/10.1002/qj.3803

Hock, R. (2003). Temperature index melt modeling in mountain areas. *Journal of Hydrology*, *282*(1–4), 104–115. https://doi.org/10.1016/S0022-1694(03)00257-9

Hock, R., Bliss, A., Marzeion, B., Giesen, R. H., Hirabayashi, Y., Huss, M., et al. (2019). GlacierMIP - A model intercomparison of global-scale glacier mass-balance models and projections. *Journal of Glaciology*, *65*(251), 453–467. https://doi.org/10.1017/jog.2019.22

Hock, R., Rasul, G., Adler, C., Cáceres, B., Gruber, S., Hirabayashi, Y., et al. (2019). Chapter 2: High Mountain Areas. IPCC special report on the ocean and cryosphere in a changing climate. 131–202.

Hood, E., Williams, M., & Cline, D. (1999). Sublimation from a seasonal snowpack at a continental, mid-latitude alpine site. *Hydrological Processes*, *13*(12–13), 1781–1797. https://doi.org/10.1002/(SICI)1099-1085(199909)13:12/13<1781::AID-HYP860>3.0.CO;2-C

Huss, M., & Hock, R. (2018). Global-scale hydrological response to future glacier mass loss. *Nature Climate Change*, *8*, 135–140. https://doi.org/10.1038/s41558-017-0049-x

Immerzeel, W. W. (2008). Historical trends and future predictions of climate variability in the Brahmaputra basin. *International Journal of Climatology*, *28*(2), 243–254. https://doi.org/10.1002/joc.1528

Immerzeel, W. W., Lutz, A. F., Andrade, M., Bahl, A., Biemans, H., Bolch, T., et al. (2020). Importance and vulnerability of the world's water towers. *Nature*, *577*(7790), 364–369. https://doi.org/10.1038/s41586-019-1822-y

Immerzeel, W. W., Pellicciotti, F., & Bierkens, M. F. P. (2013). Rising river flows throughout the twenty-first century in two Himalayan glacierized watersheds. *Nature Geoscience*, *6*(9), 742–745. https://doi.org/10.1038/ngeo1896

Immerzeel, W. W., van Beek, L. P. H., & Bierkens, M. F. P. (2010). Climate Change Will Affect the Asian Water Towers. *Science*, *328*, 1382–1385. https://doi.org/10.1126/science.1183188

Immerzeel, W. W., van Beek, L. P. H., Konz, M., Shrestha, A. B., & Bierkens, M. F. P. (2012). Hydrological response to climate change in a glacierized catchment in the Himalayas. *Climatic Change*, *110*(3–4), 721–736. https://doi.org/10.1007/s10584-011-0143-4

Jiang, Q., Li, W., Fan, Z., He, X., Sun, W., Chen, S., et al. (2020). Evaluation of the ERA5 reanalysis precipitation dataset over Chinese Mainland. *Journal of Hydrology*, *595*, 125660. https://doi.org/10.1016/j.jhydrol.2020.125660

Ji, P., & Yuan, X. (2020). Underestimation of the warming trend over the Tibetan Plateau during 1998–2013 by global land data assimilation systems and atmospheric reanalyzes. *Journal of Meteorological Research*, *34*(1), 88–100. https://doi.org/10.1007/s13351-020-9100-3

Kang, S., Xu, Y., You, Q., Flügel, W.-A., Pepin, N., & Yao, T. (2010). Review of climate and cryospheric change in the Tibetan Plateau. *Environmental Research Letters*, *5*(1), 015101. https://doi.org/10.1088/1748-9326/5/1/015101

Kaser, G., Grosshauser, M., & Marzeion, B. (2010). Contribution potential of glaciers to water availability in different climate regimes. *Proceedings of the National Academy of Sciences*, *107*(47), 20223–20227. https://doi.org/10.1073/pnas.1008162107

King, O., Bhattacharya, A., Bhambri, R., & Bolch, T. (2019). Glacial lakes exacerbate Himalayan glacier mass loss. *Scientific Reports*, *9*(1), 1–9. https://doi.org/10.1038/s41598-019-53733-x

Kirches, G., Brockmann, C., Boettcher, M., Peters, M., Bontemps, S., Lamarche, C., et al. (2014). *Land cover cci-product user guide-version 2, ESA Public Doc. CCI-LC-PUG(2.4)*.

Kraaijenbrink, P. D. A., Bierkens, M. F. P., Lutz, A. F., & Immerzeel, W. W. (2017). Impact of a global temperature rise of 1.5 degrees Celsius on Asia's glaciers. *Nature*, *549*, 257–260. [online] Available from: https://doi.org/10.1038/nature23878

Krishnan, R., Shrestha, A. B., Ren, G., Rajbhandari, R., Saeed, S., Sanjay, J., et al. (2019). Unraveling climate change in the Hindu Kush Himalaya: Rapid warming in the mountains and increasing extremes. In *The Hindu Kush Himalaya assessment* (pp. 57–97). Springer. https://doi.org/10.1007/978-3-319-92288-1_3

Lehner, B., & Grill, G. (2013). Global river hydrography and network routing: Baseline data and new approaches to study the world's large river systems. *Hydrological Processes*, *27*(15), 2171–2186. https://doi.org/10.1002/hyp.9740

Lehner, B., Verdin, K., & Jarvis, A. (2008). *HydroSHEDS*, 1–27.

Liu, J.-J., Cheng, Z.-L., & Su, P.-C. (2014). The relationship between air temperature fluctuation and Glacial Lake Outburst Floods in Tibet, China. *Quaternary International*, *321*, 78–87. https://doi.org/10.1016/j.quaint.2013.11.023

Lutz, A. F., Immerzeel, W. W., Kraaijenbrink, P. D. A., Shrestha, A. B., & Bierkens, M. F. P. (2016). Climate change impacts on the upper indus hydrology: Sources, shifts and extremes. *PloS One*, *11*, e0165630. https://doi.org/10.1371/journal.pone.0165630

Lutz, A. F., Immerzeel, W. W., Shrestha, A. B., & Bierkens, M. F. P. (2014). Consistent increase in High Asia's runoff due to increasing glacier melt and precipitation. *Nature Climate Change*, *4*(7), 587–592. https://doi.org/10.1038/nclimate2237

Marzeion, B., Hock, R., Anderson, B., Bliss, A., Champollion, N., Fujita, K., et al. (2020). Partitioning the uncertainty of ensemble projections of global glacier mass change. *Earth's Future*, *8*(7), 1–25. https://doi.org/10.1029/2019EF001470

Maurer, J. M., Schaefer, J. M., Rupper, S., & Corley, A. (2019). *Acceleration of ice loss across the Himalayas over the past 40 years*.

Merz, R., & Blöschl, G. (2004). Regionalization of catchment model parameters. *Journal of Hydrology*, *287*(1–4), 95–123. https://doi.org/10.1016/j.jhydrol.2003.09.028

Miller, J. D., Immerzeel, W. W., & Rees, G. (2012). Climate change impacts on glacier hydrology and river discharge in the Hindu Kush-Himalayas. *Mountain Research and Development*, *32*(4), 461–467. https://doi.org/10.1659/mrd-journal-d-12-00027.1

Moriasi, D. N., Arnold, J. G., Liew, M. W. V., Bingner, R. L., Harmel, R. D., & Veith, T. L. (2007). Model evaluation guidelines for systematic quantification of accuracy in watershed simulations. *Transactions of the ASABE*, *50*(3), 885–900. https://doi.org/10.13031/2013.23153

Mukhopadhyay, B., & Khan, A. (2014). A quantitative assessment of the genetic sources of the hydrologic flow regimes in Upper Indus Basin and its significance in a changing climate. *Journal of Hydrology*, *509*, 549–572. https://doi.org/10.1016/j.jhydrol.2013.11.059

Nash, J. E., & Sutcliffe, J. V. (1970). River flow forecasting through conceptual models part I - A discussion of principles. *Journal of Hydrology*, *10*, 282–290. https://doi.org/10.1016/0022-1694(70)90255-6

Na, Y., Fu, Q., & Kodama, C. (2020). Precipitation probability and its future changes from a global cloud-resolving model and CMIP6 simulations. *Journal of Geophysical Research - D: Atmospheres*, *125*(5), 1–23. https://doi.org/10.1029/2019JD031926

Nepal, S. (2016). Impacts of climate change on the hydrological regime of the Koshi river basin in the Himalayan region. *Journal of Hydro-environment Research*, *10*, 76–89. https://doi.org/10.1016/j.jher.2015.12.001

Nepal, S., Flügel, W.-A., Krause, P., Fink, M., & Fischer, C. (2017). Assessment of spatial transferability of process-based hydrological model parameters in two neighboring catchments in the Himalayan Region. *Hydrological Processes*, *31*, 2812–2826. https://doi.org/10.1002/hyp.11199

Orsolini, Y., Wegmann, M., Dutra, E., Liu, B., Balsamo, G., Yang, K., et al. (2019). Evaluation of snow depth and snow cover over the Tibetan Plateau in global reanalyzes using in situ and satellite remote sensing observations. *The Cryosphere*, *13*, 2221–2239. https://doi.org/10.5194/tc-13-2221-2019

östrem, G. (1959). Ice melting under a thin layer of moraine, and the existence of ice cores in moraine ridges. *Geografiska Annaler*, *41*(4), 228–230. [online] Available from: https://doi.org/10.1080/20014422.1959.11907953

Patil, S., & Stieglitz, M. (2014). Modeling daily streamflow at ungauged catchments: What information is necessary? *Hydrological Processes*, *28*(3), 1159–1169. https://doi.org/10.1002/hyp.9660

Pellicciotti, F., Buergi, C., Immerzeel, W. W., Konz, M., & Shrestha, A. B. (2012). Challenges and uncertainties in hydrological modeling of remote hindu kush-karakoram-himalayan (HKH) basins: Suggestions for calibration strategies. *Mountain Research and Development*, *32*(1), 39–50. https://doi.org/10.1659/MRD-JOURNAL-D-11-00092.1

Qin, Y., Abatzoglou, J. T., Siebert, S., Huning, L. S., AghaKouchak, A., Mankin, J. S., et al. (2020). Agricultural risks from changing snowmelt. *Nature Climate Change*, *10*(5), 459–465. https://doi.org/10.1038/s41558-020-0746-8

Ragettli, S., Immerzeel, W. W., & Pellicciotti, F. (2016). Contrasting climate change impact on river flows from high-altitude catchments in the Himalayan and Andes Mountains. *Proceedings of the National Academy of Sciences of the United States of America*, *113*(33), 9222–9227. https://doi.org/10.1073/pnas.1606526113

RGI Consortium (2017). *GLIMS: Global Land Ice Measurements from Space, A Dataset of Global glacier outlines version 6.0 technical report*, Colorado, USA. https://doi.org/10.7265/N5-RGI-60

Sakai, A., & Fujita, K. (2017). Contrasting glacier responses to recent climate change in high-mountain Asia. *Scientific Reports*, *7*(1), 1–8. https://doi.org/10.1038/s41598-017-14256-5

Scherler, D., Bookhagen, B., & Strecker, M. R. (2011). Spatially variable response of Himalayan glaciers to climate change affected by debris cover. *Nature Geoscience*, *4*(3), 156–159. https://doi.org/10.1038/ngeo1068

Shrestha, M., Koike, T., Hirabayashi, Y., Xue, Y., Wang, L., Rasul, G., & Ahmad, B. (2015). Integrated simulation of snow and glacier melt in water and energy balance-based, distributed hydrological modeling framework at Hunza River Basin of Pakistan Karakoram region. *Journal of Geophysical Research - D: Atmospheres*, *120*, 4889–4919. https://doi.org/10.1002/2014JD022666.Received

Singh, P., Kumar, N., & Arora, M. (2000). Degree-day factors for snow and ice for Dokriani Glacier, Garhwal Himalayas. *Journal of Hydrology*, *235*(1–2), 1–11. https://doi.org/10.1016/S0022-1694(00)00249-3

Sorg, A., Huss, M., Rohrer, M., & Stoffel, M. (2014). The days of plenty might soon be over in glacierized Central Asian catchments. *Environmental Research Letters*, *9*(10), 104018. https://doi.org/10.1088/1748-9326/9/10/104018

Stigter, E. E., Litt, M., Steiner, J. F., Bonekamp, P. N. J., Shea, J. M., Bierkens, M. F. P., & Immerzeel, W. W. (2018). The Importance of Snow Sublimation on a Himalayan Glacier. *Frontiers of Earth Science*, *6*, 1–16. https://doi.org/10.3389/feart.2018.00108

Stocker, T. F., Qin, D., Plattner, G.-K., Tignor, M., Allen, S. K., Boschung, J., et al. (2013). Climate change 2013: The physical science basis, Working Group I Contribution to the Fifth Assessment Report of the Intergovernmental Panel on Climate Change, https://doi.org/10.1017/CBO9781107415324

Strasser, U., Bernhardt, M., Weber, M., Liston, G. E., & Mauser, W. (2008). *Is snow sublimation important in the alpine water balance?*.

Terink, W., Lutz, A. F., Simons, G. W. H., Immerzeel, W. W., & Droogers, P. (2015). SPHY v2.0: Spatial Processes in HYdrology. *Geoscientific Model Development Discussions*, *8*, 1687–1748. https://doi.org/10.5194/gmdd-8-1687-2015

Wijngaard, R. R., Lutz, A. F., Nepal, S., Khanal, S., Pradhananga, S., Shrestha, A. B., & Immerzeel, W. W. (2017). Future changes in hydro-climatic extremes in the Upper Indus, Ganges, and Brahmaputra River basins. *PloS One*, *12*(12), e0190224. https://doi.org/10.1371/journal.pone.0190224

Winstral, A., & Marks, D. (2002). Simulating wind fields and snow redistribution using terrain-based parameters to model snow accumulation and melt over a semi-arid mountain catchment. *Hydrological Processes*, *16*(18), 3585–3603. https://doi.org/10.1002/hyp.1238

Yan, L., & Liu, X. (2014). Has climatic warming over the Tibetan Plateau paused or continued in recent years. *Journal of Earth, Ocean and Atmospheric Science*, *1*(1), 13–28

Yan, Z. L., Bian, Q., Xu, Z., Zhao, L., Zhang, Y. F., Zheng, H., et al. (2019). Evaluation and intercomparison of multiple snow water equivalent products over the tibetan plateau. *Journal of Hydrometeorology*, *20*(10), 2043–2055. https://doi.org/10.1175/JHM-D-19-0011.1

Yao, T., Thompson, L. G., Mosbrugger, V., Zhang, F., Ma, Y., Luo, T., et al. (2012). Third pole environment (TPE). *Environmental Development*, *3*(1), 52–64. https://doi.org/10.1016/j.envdev.2012.04.002

Zandler, H., Haag, I., & Samimi, C. (2019). Evaluation needs and temporal performance differences of gridded precipitation products in peripheral mountain regions. *Scientific Reports*, *9*(1), 1–15. https://doi.org/10.1038/s41598-019-51666-z

Zhang, G., Yao, T., Xie, H., Wang, W., & Yang, W. (2015). An inventory of glacial lakes in the Third Pole region and their changes in response to global warming. *Global and Planetary Change*, *131*, 148–157. https://doi.org/10.1016/j.gloplacha.2015.05.013

Zhang, Y., Liu, S., & Ding, Y. (2006). Observed degree-day factors and their spatial variation on glaciers in western China. *Annals of Glaciology*, *43*, 301–306. https://doi.org/10.3189/172756406781811952

Zhan, Y.-J., Ren, G.-Y., Shrestha, A. B., Rajbhandari, R., Ren, Y.-Y., Sanjay, J., et al. (2017). Changes in extreme precipitation events over the Hindu Kush Himalayan region during 1961-2012. *Advances in Climate Change Research*, *8*(3), 166–175. https://doi.org/10.1016/j.accre.2017.08.002

Zscheischler, J., Martius, O., Westra, S., Bevacqua, E., Raymond, C., Horton, R. M., et al. (2020). A typology of compound weather and climate events. *Nature Reviews Earth & Environment*, *1*, 333–347. https://doi.org/10.1038/s43017-020-0060-z

Zscheischler, J., & Seneviratne, S. I. (2017). Dependence of drivers affects risks associated with compound events. *Science Advances*, *3*(6), e1700263. https://doi.org/10.1126/sciadv.1700263

Zscheischler, J., Westra, S., Van Den Hurk, B. J. J. M., Seneviratne, S. I., Ward, P. J., Pitman, A., et al. (2018). Future climate risk from compound events. *Nature Climate Change*, *8*(6), 469–477. https://doi.org/10.1038/s41558-018-0156-3